University of Alabama in Huntsville
LOUIS

Theses

UAH Electronic Theses and Dissertations

2024

Evaluating the effects of L-PBF printing parameters on the microstructure and mechanical properties of GRCop-42

Elaina Walker

Follow this and additional works at: https://louis.uah.edu/uah-theses

Recommended Citation

Walker, Elaina, "Evaluating the effects of L-PBF printing parameters on the microstructure and mechanical properties of GRCop-42" (2024). *Theses*. 656.
https://louis.uah.edu/uah-theses/656

This Thesis is brought to you for free and open access by the UAH Electronic Theses and Dissertations at LOUIS. It has been accepted for inclusion in Theses by an authorized administrator of LOUIS.

EVALUATING THE EFFECTS OF L-PBF PRINTING PARAMETERS ON THE MICROSTRUCTURE AND MECHANICAL PROPERTIES OF GRCOP-42

Elaina Walker

A THESIS

Submitted in partial fulfillment of the requirements
for the degree of Master of Science
in
The Department of Mechanical and Aerospace Engineering
to
The Graduate School
of
The University of Alabama in Huntsville
May 2024

Approved by:

Dr. Judith Schneider, Research Advisor
Dr. Nathan Spulak, Committee Member
Dr. Joseph Sims, Committee Member
Dr. Paresh Samantaray, Committee Member
Dr. George Nelson, Department Chair
Dr. Shankar Mahalingam, College Dean
Dr. Jon Hakkila, Graduate Dean

Abstract

EVALUATING THE EFFECTS OF L-PBF PRINTING PARAMETERS ON THE MICROSTRUCTURE AND MECHANICAL PROPERTIES OF GRCOP-42

Elaina Walker

A thesis submitted in partial fulfillment of the requirements for the degree of Master of Science

The Department of Mechanical and Aerospace Engineering

The University of Alabama in Huntsville
May 2024

GRCop-42 is a dispersion strengthened copper alloy of interest due to its high thermal conductivity. Since it is fabricated as a powder, it is adaptable to powder based, metal additive manufacturing (AM) processing. The chromium-niobium additives phase separate from the copper matrix and form strengthening dispersoids during the gas atomization process used to produce the powder. This study looks at the effect of the powder based, laser powder bed fusion (L-PBF) AM processing parameters on the resulting microstructure and mechanical properties. Builds were obtained from five different vendors, deposited using their best practice, for metallurgical and mechanical property evaluation. By comparing the size, morphology, and distribution of the dispersoids with the resulting mechanical properties, the consistency of the process across multiple platforms can be evaluated. This information is critical for establishing standards for the material properties in metal AM parts of GRCop-42.

Acknowledgements

Funding was provided by the Alabama Research and Development Enhancement Fund (ADECA) and a NASA MSFC summer internship with EM31.

The work described in this thesis would not have been possible without the assistance of many people who deserve recognition. Firstly, I would like to thank Dr. Judy Schneider for her patience and guidance in both the lab and classroom. The opportunities and lessons you have given me will always be remembered. Secondly, the EM31 team at NASA MSFC. Everyone there treated me as an equal and provided me with the equipment and techniques necessary to further expand my studies. Finally, the members of my committee who have provided me with helpful comments and suggestions.

I would like to thank my fiancé and my family who have provided their unwavering support, understanding, and encouragement through my pursuit of this degree.

Table of Contents

List of Figures

List of Tables

Chapter 1. Introduction

The use of powder metallurgy (PM) can be dated back as far as 3000 BC where it is reported that Egyptians used a crude form of iron PM to craft daggers while the Incas used powdered precious metals to fabricate jewelry and other artifacts [1,2]. The mass manufacturing of PM products did not begin, however, until the mid- to late nineteenth century with the production of items such as copper coins, tungsten wires, and platinum ingots [3]. Rapid growth in PM technology occurred post-WWII as PM entered the automotive industry which resulted in iron and steel becoming the most used PM material [3]. It was not until the 1960's that fully dense products were developed due to the accelerated demand for high-performance super alloy in aircraft turbine engine parts [3]. The traditional methods to achieve a fully dense PM part includes creating the powder, compacting the power into a metal billet, and sintering and/or forging the billet to further consolidate the powder. This process generates a fully dense piece of material that then may undergo additional subtractive machining to achieve its final net shape.

Powders developed for PM can now be used in metal additive manufacturing (AM) processing. This provides the ability to directly build complex, net shapes that require minimal post-production processing. This can reduce production time and cost, for production of low volume, complex parts.

1.1 Motivation

More companies are designing and selling metal additive manufacturing (AM) machines for commercial use, which is reflective of the growing interest in the AM processes. The AM process is a desirable tool as it can lower the cost to produce low volume, complex parts. As a result, more fabrication houses are incorporating AM technology into their production lines; However, standardization for AM processing is still being developed and an understanding of the critical parameters is needed to support this effort. Each machine and its operator are unique and as a result, the material properties of the resulting component may differ. Within the limitations of each AM device, there are an array of processing parameters that are optimized for consolidation of a variety of alloys. These parameters, some of which are depicted in Figure 1.1, can include laser type and power, scan speed, layer thickness, scan strategy, hatch spacing, gas type and flow rate and spot size. To increase the predictability of the material properties of AM materials, it is important to analyze how these different processing parameters influence the resulting microstructure and hence mechanical properties.

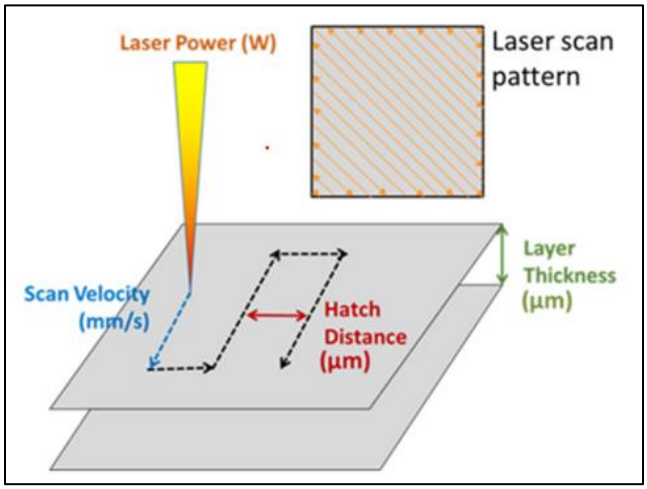

Figure 1.1: Schematic for L-PBF Processing Parameters [4].

1.2 Objective of Study

This study is focused on the AM process of laser-powder bed fusion (L-PBF) using GRCop-42, a dispersion strengthened copper alloy. To evaluate possible differences in the L-PBF material, a standardized build design was sent to five different vendors for printing, each using their company's best practices. By analyzing the differences in dispersoid size and distribution among the specimens, and comparing back to the provided printing parameters, the robustness of the L-PBF process can be evaluated for GRCop-42 components across multiple platforms.

Chapter 2. Background

2.1 Copper Alloys

Copper (Cu) is used in high heat flux applications due to its high thermal conductivity. Although Cu is a great conductor, in its unalloyed form it is low in strength therefore limiting its applications. Among the considerations for various Cu alloys are the tradeoffs between temperature dependent strength and thermal conductivity. Table 2.1 summarizes some of the more common Cu alloys used in the aerospace field. The nominal elemental compositions of the mentioned alloys are provided in Table 2.2. Cu alloys listed in Table 2.1 that rely on coherent precipitation strengthening have an upper limit on the operating temperature to avoid over aging and thereby losing strength. Dispersion strengthened alloys offer the advantage of higher operating temperatures due to their incoherent particles that are not affected by over aging [5].

Table 2.1: Summary of Strength and Conductivity for Various Cu Alloys.

Alloy	Primary Strengthening Mechanism	Ultimate Tensile Strength (MPa)	Yield Strength (MPa)	Thermal Conductivity (W/m*K)
C18200-TB00 [6]	Precipitation	310	97	171
C18150 [7]	Precipitation	469	338	26.9
AMZIRC [8,9]	Cold work	450	350	367
NARloy-Z [8,10]	Precipitation	315	138	296
GlidCop[7,8]	Dispersion	464	184	365
GRCop-84 [10,11]	Dispersion	400	225	280
GRCop-42 [10,11]	Dispersion	350	200	344
Copper [7]	-	210	33	385

Table 2.2: Cu alloy compositions (wt %).

Alloy	Cu	Cr	Nb	Ag	Zr	Al	O
C18200 [6]	99.1	0.9	-	-	-	-	-
C18150 [8]	98.9	1.0	-	-	0.1	-	-
AMZIRC [8]	99.85	-	-	-	0.15	-	-
NARloy-Z [8]	96.5	-	-	3.0	0.5	-	-
GlidCop [8]	99.68	-	-	-	-	0.15	0.17
GRCop-84 [9]	88.4-87.2	6.2-6.8	5.4-6	-	-	-	-
GRCop-42 [9]	94.2-93.6	3.1-3.4	2.7-3	-	-	-	-

2.2 The Laser Powder Bed Fusion (L-PBF) Process

A schematic of the L-PBF process is shown in Figure 2.1. For this AM method, a 3D model is sliced into layers where each layer of the sliced model is one deposition layer in the print. To accommodate overhangs, adequate support structure may be added. Prior to printing each layer, the roller evenly distributes a layer of powder across the substrate and the laser then traces the geometry of the sliced layer and consolidates the powder. Once one layer is completed, the fabrication piston is lowered, and the process begins again on the next layer.

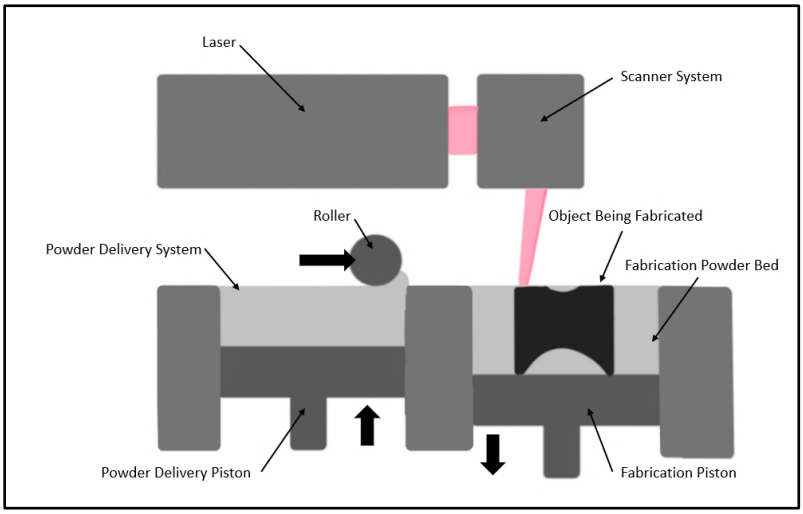

Figure 2.1: Schematic for L-PBF Process [12].

The quality of the consolidated material is governed by a variety of parameters such as laser power, scan speed, hatch spacing, and layer thickness. Using these values, the energy

density can be calculated as described in Equation 1 where P is the laser power, v is the scan speed, h is the hatch spacing, and t is the layer thickness:

$$Energy\ Density\ \left(\frac{J}{mm^3}\right) = \frac{P}{vht}\,. \tag{1}$$

2.3 Powder Production

Many fabrication methods utilize powder such as: PM, L-PBF, or plasma spraying [9,13]. Powders produced for these processes rely on rapid solidification through an atomization process. A conventional gas atomization process is shown in Figure 2.2, with either Argon or Nitrogen as the gas source.

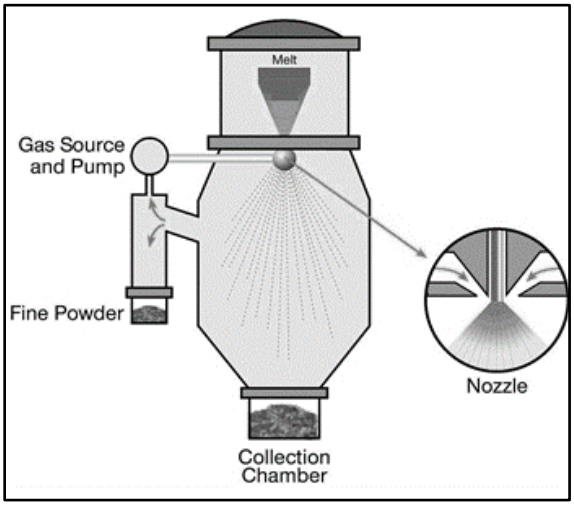

Figure 2.2: Schematic of Argon Gas Atomization [14].

Gas atomization begins by melting an alloy in the melting chamber. The melt is then directed through a nozzle which forms a melt stream. A gas is then directed toward the stream which forms a distribution of particle sizes. The particles then begin to fall and solidify in the spray chamber. These solidified particles are then collected on a metal collection plate [15]. Once the powder is formed, it is sieved per the required size distribution.

2.4 Strengthening Mechanisms

Strengthening of alloys can be obtained by a variety of mechanisms. Alloying elements can be added to either promote solid solution strengthening, precipitation strengthening or dispersion strengthening. In addition, if the grains can be refined, the strength will increase with decreasing grain size. Of these, solid solution, grain size, and dispersion strengthening can retain their strength, whereas precipitation strengthening loses its effectiveness at elevated temperatures [5,16]. This section covers the strengthening mechanism of interest to the Cu alloys.

2.4.1 Precipitation Strengthening

Of the strengthening mechanisms, precipitation of coherent second phase particles produce the highest strength alloy. Precipitation strengthening is a strengthening mechanism used in alloys that have limited solid solution solubility at room temperature and increased solubility at elevated temperatures[5]. By applying a post fabrication heat treatment to the alloy, the second phase can be precipitated out of solid solution and into the matrix. A typical heat treatment for a precipitation strengthened alloy includes a solution treatment to dissolve all solutes, followed by a quench in which the matrix becomes super saturated. After quenching, the material can be artificially aged by heating to a temperature below the solvus temperature. During the ageing treatment nano sized second phase particles will precipitate out of solid solution and into the matrix[5,13,17]. Larger temperature differentials will result in a higher rate of nucleation but lower growth rate resulting in numerous fine precipitates [5,18]. A smaller temperature differential will result in a lower rate of nucleation but with a higher growth rate that results in fewer, larger, precipitates. The precipitates provide strengthening by forming particles that remain coherent with the matrix [13,18]. The use of precipitation strengthened alloys is

limited in operation at elevated temperatures since the precipitates can coarsen, thereby losing their coherency and their ability to strengthen the matrix effectively[5].

C18200, C18150, AMZIRC, and NARloy-Z listed in Tables 2.1 and 2.2 are strengthened by the precipitation of various nano sized second phase particles. C18200 and C18150 are alloys that obtain their strengthening through the precipitation of nano sized Cr particles or nano sized Cr particles and the Cu_xZr phase respectively[8]. The strength of these alloys can be further increased by cold working. At extended time at elevated temperatures, both cold working and precipitation hardening lose their effectiveness [13].

The Cu-Cr phase diagram is shown in Figure 2.3 and the Cu-Zr phase diagram in Figure 2.4. There is limited solubility of Cr and Zr into the Cu matrix with a maximum of 0.73 wt.% at 1084 ℃ and a maximum of 0.127 wt.% at 972 ℃ respectively.

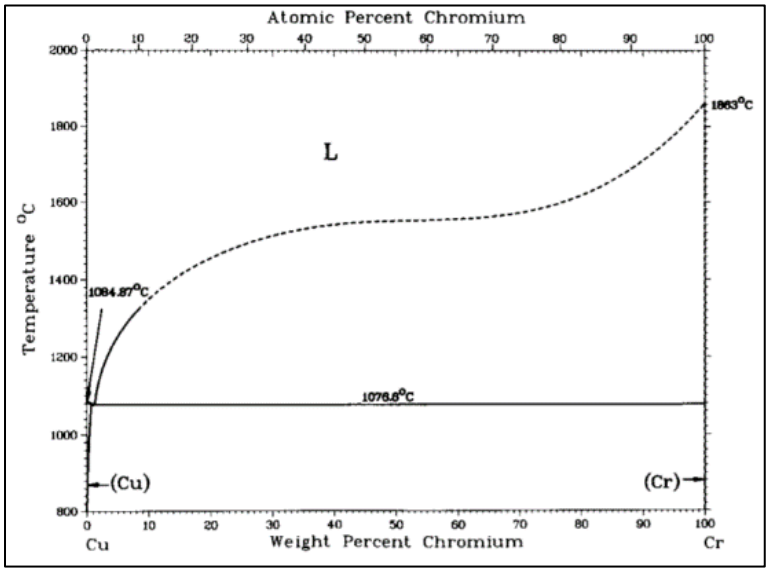

Figure 2.3: Cu-Cr Phase Diagram [19].

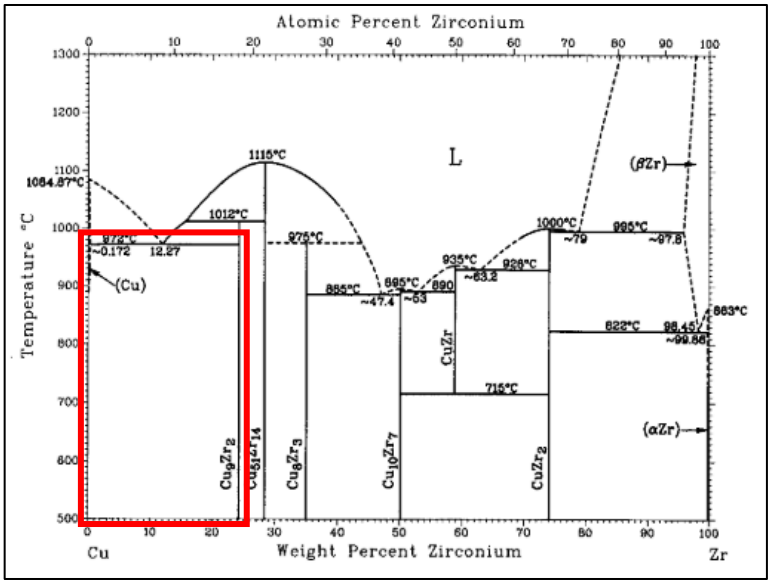

Figure 2.4: Cu-Zr Phase Diagram [19].

Due to the limited solid solution solubility of Cr into Cu, only small amounts of Cr can be added to the Cu to provide strengthening which allows C18200 to retain some of its thermal conductivity when compared to pure Cu. The addition of Zr in C18150 allows for the formation of Cr precipitates and a Cu_xZr phase which improved the tensile strength when compared to C18200 at the cost of its thermal conductivity.

Although sufficient for spot welding electrode material, C18200 could not meet the requirement for reusability in high heat flux applications due to short creep and fatigue life [20]. The creation of C18150 though the addition of Zr saw an improved creep life, however the push for a reusable Cu alloy that can operate in high heat flux environments with improved creep resistance and an improved fatigue life led to the creation of AMZIRC and NARloy-Z.

AMZIRC is a Cu-Zr alloy that obtains approximately 80% of its strengthening from cold working and the remainder from the precipitation of micron sized Cr_xZr intermetallic particles, or dispersions, that pin grain boundaries and slow grain boundary growth [8]. The Cu-Zr phase diagram shown in Figure 2.4 highlights the limited solubility of Zr in the Cu matrix with a maximum of 0.172 wt% at 972 °C as well as the mixture region which is composed of Zr and Cr_xZr intermetallic phases indicated by the red box. Although AMZIRC was able to meet the conductivity, fatigue and creep resistance requirements, further development of the NARloy-Z demonstrated longer and more uniform cycle lifetimes under realistic loading conditions [8].

NARloy-Z is a precipitation strengthened Cu alloy whose strength also relies on the formation of the Cr_xZr intermetallic dispersions which form on grain boundaries and adds the precipitation of Ag particles throughout the matrix for strengthening [8,9,21]. The Ag-Cu phase diagram shown in Figure 2.5 highlights the increased solubility of Ag in the Cu matrix with a maximum of 8.8 wt.% at 779°C and the Zr-Cu phase diagram in Figure 2.3 highlights the mixture region of Zr and Cr_xZr intermetallics.

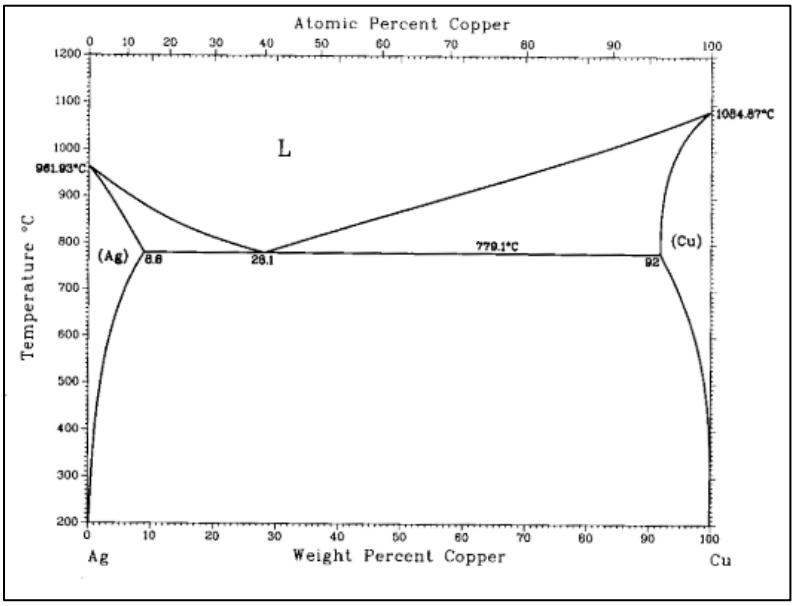

Figure 2.5: Ag-Cu Phase Diagram[19].

Although NARloy-Z meets the requirements for creep and fatigue life, because it is precipitation strengthened, extended time at temperature above 592 ℃ results in coarsening of the Ag precipitates which degrades the material properties [10].

2.4.2 Dispersion Strengthening

Dispersion strengthening is a strengthening mechanism that is used in alloys in which the second phase alloying elements exceed the maximum solubility with the matrix. The resulting strength from the incoherent second phase particles rely on the size of the dispersoid, their nearest neighbor distances, and location within the matrix [13,17]. There are a few methods to obtain this dispersion arrangement which include, mixing the particles directly into the molten metal during casting, precipitation of the dispersions, phase separation, or mechanical alloying [13].

GlidCop is an oxide dispersion strengthened alloy which obtains its strength from the introduction of nano sized Al_2O_3 dispersoids. This alloy is generated via high-energy planetary fast milling of Cu and Al_2O_3 powders to obtain a fine distribution of Al_2O_3 oxides throughout the Cu matrix [22]. Because it is dispersion strengthened, it can retain its strength when subjected to extended time at elevated temperatures.

The GRCop family of alloys are dispersion strengthened Cu alloys with the binary phase diagrams for Nb and Cr with Cu shown in Figure 2.6 and Figure 2.7, respectively. The designations of 84 and 42 refer to the atomic percentage of the alloying elements with 42 having half that of 84. Both Cr and Nb have negligible solubility in the Cu matrix. This simply means that minimal amounts of the Cr and Nb will not go into solution with the Cu and will instead remain separate from the Cu matrix.

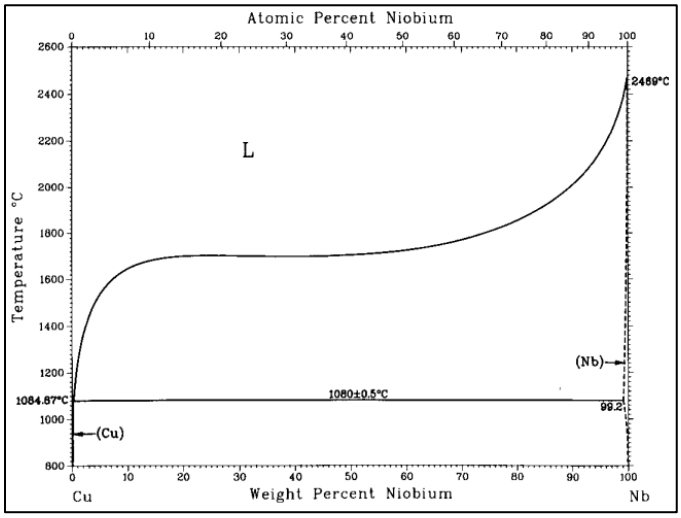

Figure 2.6: Cu-Nb Phase Diagram [19].

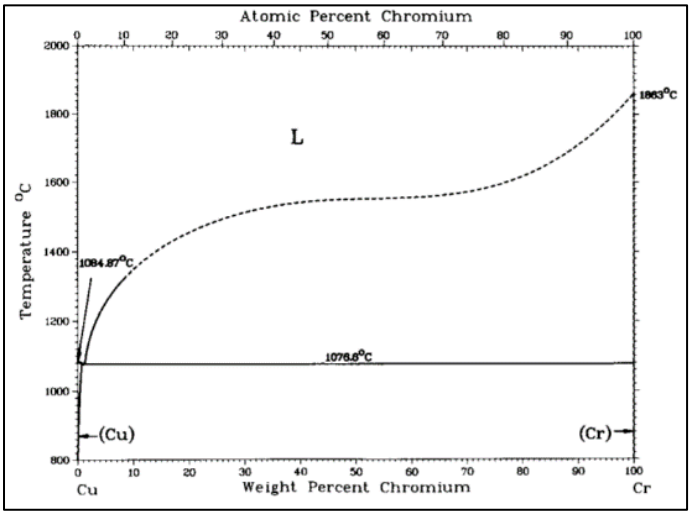

Figure 2.7: Cu-Cr Phase Diagram [19].

Due to negligible solubility, Cr and Nb phase separate to form the Cr_2Nb intermetallic. Figure 2.8 shows the equilibrium phase diagram for Cr-Nb. Thus, the strengthening in this alloy system comes from the Cr_2Nb intermetallics which form incoherent dispersoids in the Cu alloy system [8].

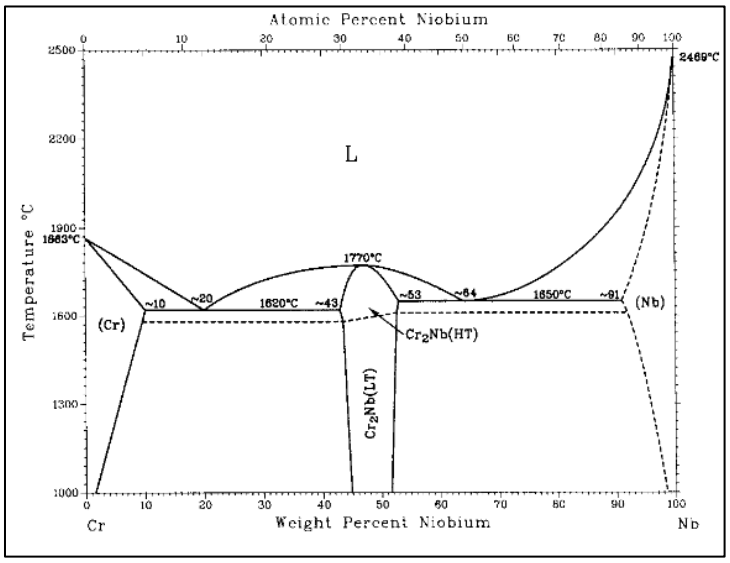

Figure 2.8: Cr-Nb Phase Diagram[19].

The dispersions strengthen the alloy by acting as dislocation and grain boundary pinners [8]. The Cr_2Nb dispersion is stable at elevated temperatures as can be observed by comparing its melting temperature of 1770 °C to the melting temperature of Cu of 1084 °C. Thus, if the Cr_2Nb dispersions form at grain boundaries, they slow grain growth at elevated temperatures up to operating temperatures of 1650 °C [8,23]. Their lack of solubility also allows GRCop-84/42 to retain its high thermal conductivity due to the purity of the Cu matrix [24]. Studies have shown that the Cr_2Nb dispersions resist coarsening at temperatures of 1000 °C for up to 20 hours [9,12,25].

2.5 GRCop-42 Strengthening Mechanisms

Solution, dispersion, grain size and precipitation strengthening all rely on inclusions within the matrix that form strain fields that impede dislocation motion. Additionally, the formation of either precipitates or dispersoids along grain boundaries restricts grain growth at elevated temperatures [5,13,18].

2.5.1 Grain Size Strengthening

Grain size strengthening is described by the Hall-Petch relationship and relies on decreasing the average grain size thereby increasing the stress necessary to move a dislocation across an increased number of grain boundaries[5]. The empirically derived Hall-Petch equation can be used to determine the relationship between the yield stress and the grain size of the material. This relationship is shown in Equation 2 where σ_y is the yield strength, σ_0 is a material constant for the threshold stress for dislocation motion, k_y is the material dependent strengthening coefficient, and d is the average grain diameter [16]. The Hall-Petch relationship is valid up to grain size of 100 µm and breaks down at grain sizes less than 1 µm [5,26]:

$$\sigma_y = \sigma_0 + \frac{k_y}{\sqrt{d}}. \quad (2)$$

2.5.2 Dispersion Strengthening

The role of dispersions in strengthening of alloys relies on internal strain fields to impede dislocation motion through the matrix [5]. Under external loads, the energy required for a dislocation to pass through the material is increased as local elastic strain fields are encountered making the material stronger [13]. Internal strain fields associated with second phase particles are due to either coherent or incoherent interface with the matrix. Nano-scale particles that precipitate out of the matrix during artificial aging, are coherent with the matrix. In contrast, dispersoids are typically micron-scale particles that are incoherent with the matrix material [5]. As dislocations interact with smaller, coherent particles they will eventually cut through the particle. As the particles become larger and lose their coherency, the dislocation line will be pinned and eventually bow around the particles to pass through[17,27]. Figure 2.9 illustrates the rate controlling mechanisms for increasing strength as a function of particle size changing from a shearing to bowing mechanism.

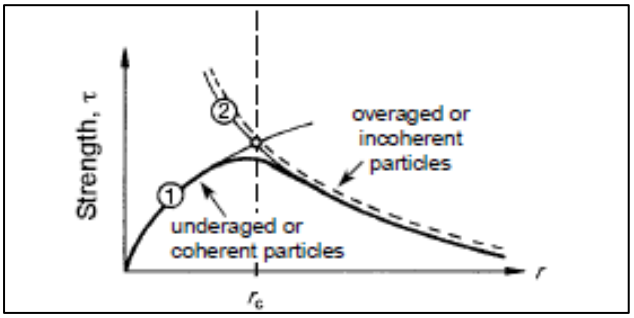

Figure 2.9: Strengthening as a Function of Particle Size. Particle Shearing Occurs up until Peak Strengthening Occurs at which Dislocation Bowing Begins [5].

As a dislocation travels through the material, if the particles are large enough to withstand a shear force strong enough to bow the dislocation, the dislocation will bow around the particle and leave behind dislocation loops as shown in Figure 2.10. The dislocation bowing is referred to as Orowan strengthening. If the particle is too small, the dislocation will instead shear

the particle resulting in a faulted plane as shown in Figure 2.11 and is referred to a Friedel cutting. The dislocation loops are theorized to result in increased dislocation density as described by Frank-Reed source as well as reducing the distance between particles [13,17].

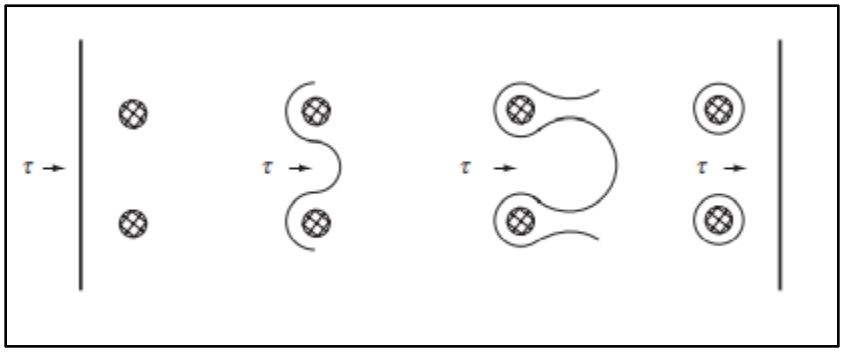

Figure 2.10: The Orowan Model of Dislocation Bowing Leading to Increased Strength [13].

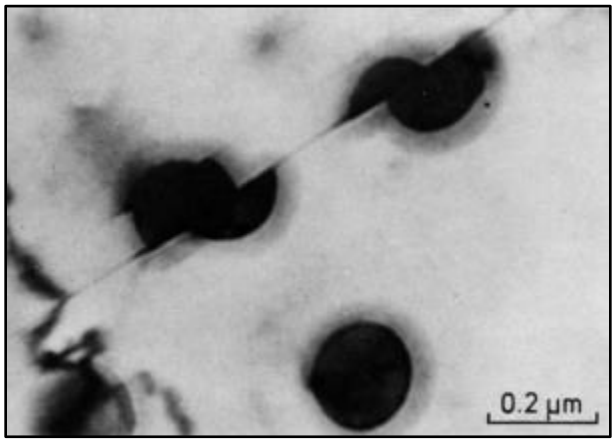

Figure 2.11: Example of Smaller Particles Subjected to Shearing[13].

Orowan's equation describes the relationship between the applied stress and the dislocation bowing and is shown in Equation 3 where $\Delta\tau_y$ is the increase in yield stress due to the particles, G is the shear modulus and x is the particle spacing [28]:

$$\tau_{orowan} = \frac{Gb}{x}. \quad (3)$$

Ashby further developed this equation to address the interparticle spacing and the effects of statistically distributed particles which resulted in the creation of the Ashby-Orowan model shown in Equation 4 where $\Delta\sigma_y$ is the increase in yield strength, G is the shear modulus, b is the

burgers vector, f is the volume fraction of particles, and r is the average radius of the particles [28]:

$$\Delta\sigma_y = 0.538Gb\left(\frac{\sqrt{f}}{2r}\right)\ln\left(\frac{r}{b}\right). \quad (4)$$

Chapter 3. Experimental Procedure

3.1 Specimen Layout

The layout of the eight build plates received from six different vendors is shown in Figure 3.1. Although a variety of specimens were printed, only those circled were evaluated in this study. Specimens were taken from each build plate for microscopy and mini-tension testing. Figure 3.1 indicates the location of these two regions, in the red oval, the specimens for microscopy, and in the white oval, the specimens for mini-tension testing. A heritage specimen that was directly extruded is also included in the study as a point of comparison for the L-PBF specimens.

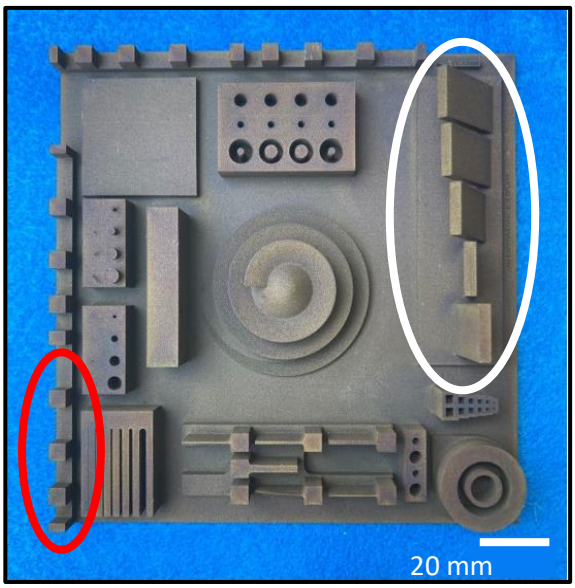

Figure 3.1: Sample Build Plate. The White Oval Indicates Location of Mini-Tension Test Samples, and the Red Oval Indicates Location of Microscopy samples.

3.2 Build Parameters

Each vendor printed the plates using L-PBF printers according to their best practices which are summarized in Table 3.1. The feedstock material was GRCop 42 powder procured by each

vendor with a nominal size of 10-45 µm. After printing each build plate underwent hot isostatic processing (HIP). Generally, for copper alloys, HIP is performed at 800-950°C under a pressure of 100 MPa [29].

Table 3.1: Provided Vendor Printing Parameters.

Identifier	Machine	Energy Density (J/mm^3)	Scan Strategy	Recoater Blade
A-1	EOS M280	75.0	Continuous	Rubber
A-2	EOS M280	75.0	Continuous	Steel
B-1	EOS M290	90.3	Stripes	Steel
B-2	EOS M400-1	83.3	Stripes	Steel
C	EOS M400-1	75.0	Continuous	Rubber
E	EOS M400-4	83.3	Stripes	Steel
F	EOS M290	90.3	Unavailable	Carbide

3.3 Optical Microscopy

Of the three microscopy specimens indicated in Figure 3.1, one was used for observation of the XY plane (build plane) and the second for observation of the Z plane (build direction). These specimens were nominally 5 mm by 5 mm by 8 mm and were removed from the build plate by using a water-cooled abrasive saw. A directly extruded specimen, machined for Charpy testing, in Figure 3.2, provided the specimen for analysis. The extruded direction and transverse direction were cut for observation.

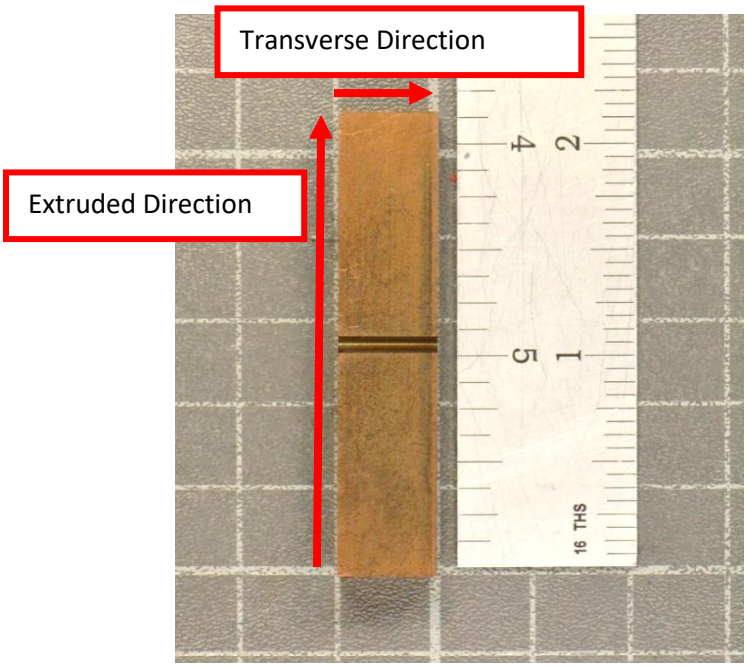

Figure 3.2: Directly Extruded Specimen.

To prepare for microscopy preparation, each orientation is mounted in a black phenolic using the hot mounting press with the following settings:

Heat Time: 6 min

Cool Time: 4 min

Pressure: 6.8 kPa

Temperature: 180 ℃

Once mounted, all specimens were ground using a series of SiC grinding pads ranging from 320 to 1200 grit. Final polishing used a series of diamond suspension polishing mediums ranging from 3 µm to 0.05 µm with vel-cloth polishing pads on a Struers auto polisher. The preparation schedule is summarized in Table 3.2. The specimens were determined to be ready for imaging when the surface appeared mirror like to the naked eye with no large scratches apparent. Images of the polished specimens were recorded using a Leica optical microscope at a magnification of 500x and 1000x to characterize the size, morphology and spacing of the dispersoids.

Table 3.2: Polishing Schedule for Microscopy Samples.

Grit	Pressure	Time
320	15 N	1 min
400	15 N	1 min
500	15 N	1 min
600	15 N	1 min
800	15 N	3 min
1200	15 N	3 min
3 µm	20 N	10 min
1 µm	20 N	10 min
0.05 µm	20 N	3 min

To reveal the grain structure, the specimens were etched using Waterless Kallings. The specimens were submerged in the solution for 2 seconds then promptly rinsed and cleaned with acetone and methanol. Images were again taken with the Leica microscope at a magnification of 500x to characterize the grain structure and second phase dispersoids.

3.4 Scanning Electron Microscopy (SEM)

Higher resolution images were obtained using a MAIA3 TESCAN SEM in secondary electron imaging (SEI) mode at a magnification of 20.0kx with a working distance of 15 mm, located at the NASA Glenn Research Center. To prepare for imaging, each sample was repolished to remove the etchant using the polishing schedule in Table 3.2.

3.5 Tension Testing

Four mini-tension specimens were machined from three of the overhang walls circled in white on the build plate in Figure 3.1. The angles of interest are the 45°, 60°, and 90° with nominal dimensions of 25 mm by 14 mm by 2.5 mm. These angles are referred to as overhangs and refer to the orientation of the build with respect to the build plate. The specimens were cut

using wire EDM according to the layout in Figure 3.3 with individual specimen dimensions shown in Figure 3.4. The final thickness of the tensile specimens was machined to 2.2 mm.

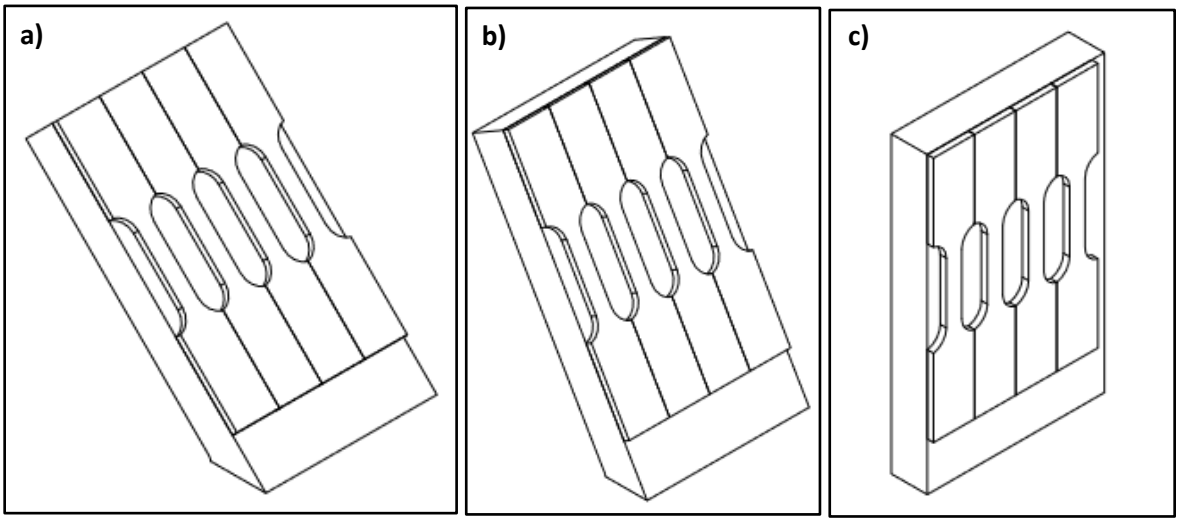

Figure 3.3: Cut Plan Layout for tensile specimens: a) 45° b) 60° c) 90 °.

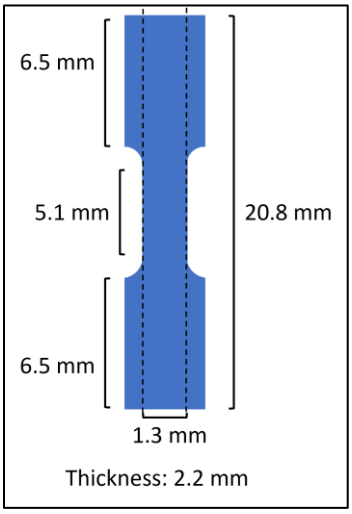

Figure 3.4: Dimensions of Mini-Tension Specimens (dimensions shown in mm).

The mini-tension testing was conducted by Touchstone Labs using a 22 kN load cell with an initial test strain rate of 0.015 mm/mm/min switching to a second test speed of 25 mm/min at 5% strain [30]. The Epsilon Model# 3442-004M-020M-LHT extensometer had a gauge length of 4 mm. The raw data of load, strain and time was used to calculate the yield strength, ultimate tensile strength, and elongation at failure.

3.6 Dispersion Analysis

SEM images obtained from the NASA Glenn Research Center were analyzed using ImageJ analysis. Images received were converted to an 8-bit image in greyscale which was then thresholded to black and white[31]. The images were taken at a magnification of 20kx. The measurements recorded were the area fraction (nominally 7%), the feret diameter, and the nearest neighbor distance of the dispersoids. Any particles with an area smaller than 0.0007 μm (2 x 2 pixel area) were excluded in the final calculations. Approximately 5000 dispersoids were analyzed per image. An image from each the XY and the Z orientations were analyzed.

3.7 Fractography

As a load drop of 40% was used to terminate the tests at Touchstone Labs, many specimens were still partially connected. Thus, to examine the fracture surfaces, the specimens were pulled completely apart using an Instron electro-mechanical load frame with fracture surfaces preserved. For initial observation of the fracture surfaces, a Keyence VHX-7000 series digital microscope was used. Using the z-stack function, 3D images of the fracture surface were generated to provide an overview of the fracture surface. For higher resolution imaging, a Hitachi-S3700N SEM was used. Images were taken in secondary electron imaging mode (SEI) with an excitation voltage of 15 kV and a working distance of approximately 10 mm.

3.8 Electron Backscatter Diffraction

Electron Backscatter Diffraction (EBSD) was conducted at the NASA Glenn Research Center with a TESCAN MAIA-3 SEM operated at 20 kV using an Oxford Nordlys Nano EBSD detector for information on the grains. Images were montaged to obtain a total field of view of 1

mm wide by 0.7 mm tall. A step size of 1 μm was used with grains as defined by a minimum grain misorientation angle of 3° and a minimum of 10 pixels. Prior to observation specimens were polished using the procedure described in Table 3.2. Post processing was performed using AZtec software to generate an EBSD map. To minimize computational time only Cu was indexed.

3.9 X-Ray Diffraction

X-ray diffraction (XRD) was performed with a Malvern Panalytical Empyrean with a 255 channel detector to determine the phases present in a representative L-PBF sample and DE sample. XRD patterns were collected with an Empyrean detector with Co-Kα radiation with an average wavelength of 1.79 nm. A 20°-120° two-theta range was scanned with a step size of 0.0131° and a scan speed of 1194.42 seconds per step. Slow scans were used to reveal minor phases.

Chapter 4. Results

4.1 Optical Microscopy

Polished sample images obtained from optical microscopy were used to characterize volumetric voids and dispersions in the sample. The images for qualitative analysis of the volumetric voids and dispersoids were taken at a magnification of 500x and 1000x respectively. Representative images in the polished state in both the XY and Z planes for each of the vendors are shown below in Figure 4.1 and Figure 4.2 respectively. For comparison, a representative image for both the extruded direction and transverse direction of a directly extruded sample are included in Figure 4.3. Most dispersoids, as indicated by the arrows, for the L-PBF samples are 1 μm in diameter or smaller except for a few larger dispersoids approximately 5 μm in diameter. The Cu rich regions indicated by circles provides evidence for lack of fusion defects in both the XY and Z planes for specimens C and A-2 that were assumed to be sealed after the HIP operation. In the directly extruded material, the dispersoids appear uniform in size and distribution across both directions.

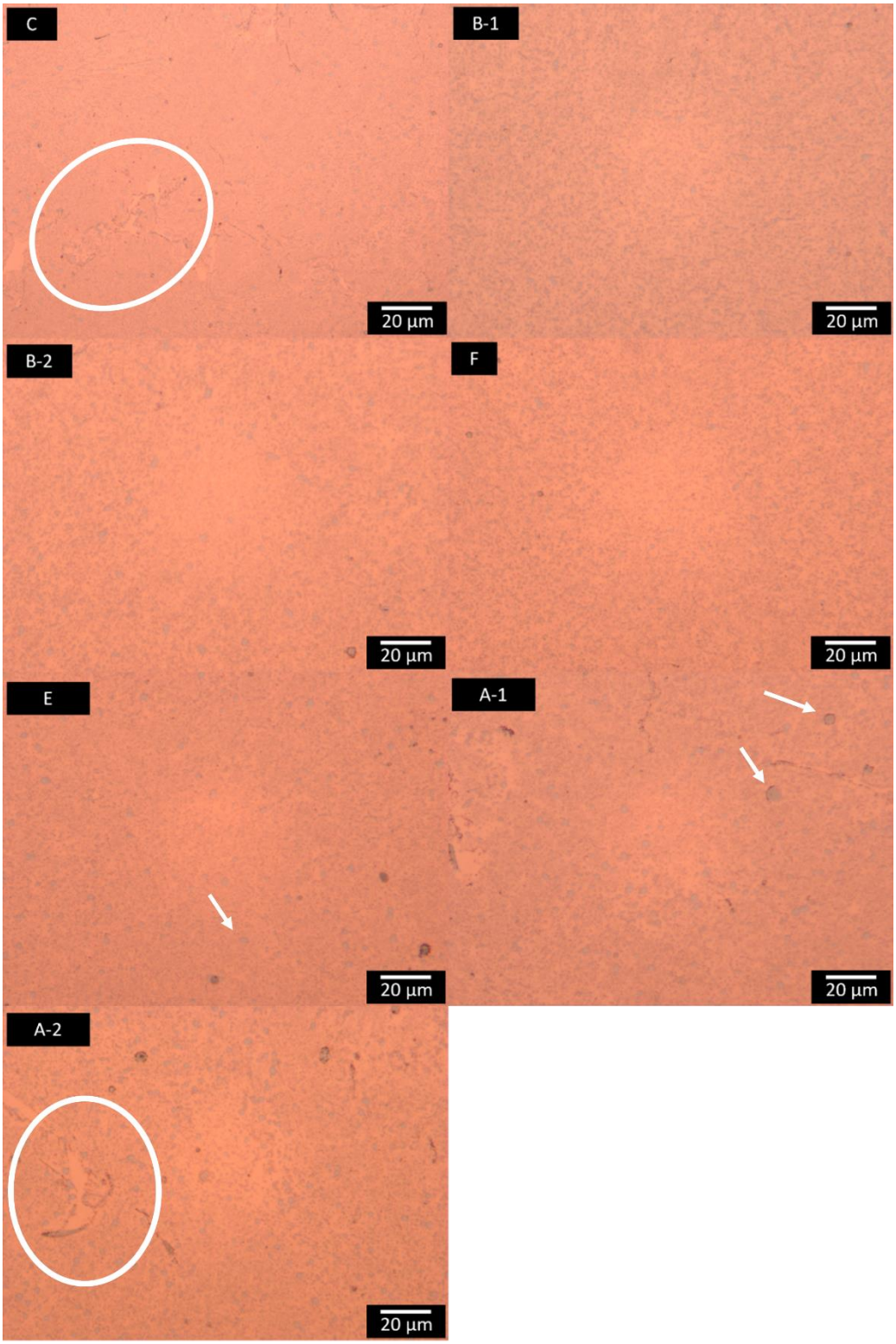

Figure 4.1: Representative Images for Each Vendor in the XY Plane. Circles showing Cu rich regions and arrows showing the larger dispersoids. Specimen ID in upper corner of each image.

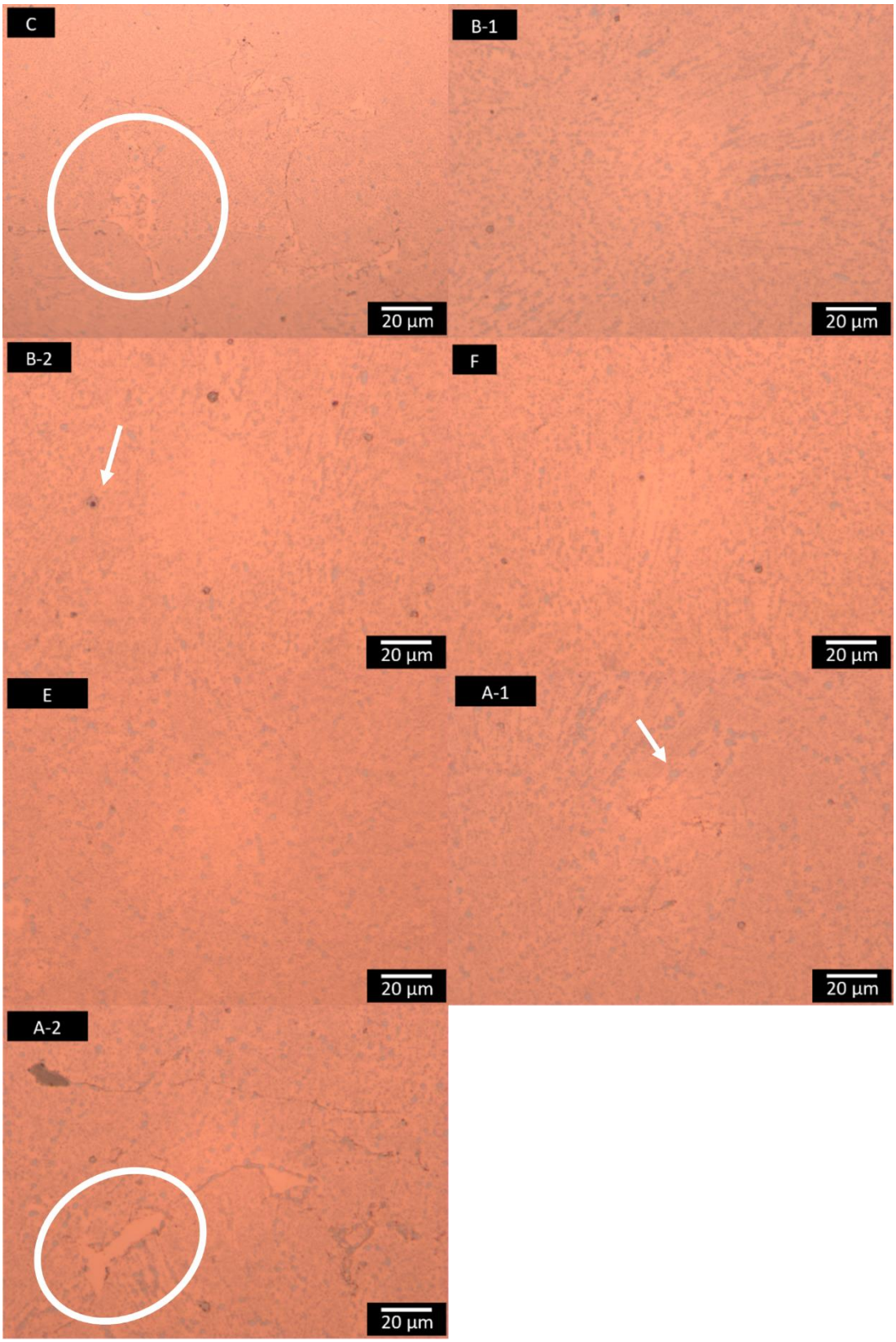

Figure 4.2: Representative Images for Each Vendor in the Z Plane. Circles showing Cu rich regions with arrows showing the larger dispersoids. Specimen ID in upper corner of each image.

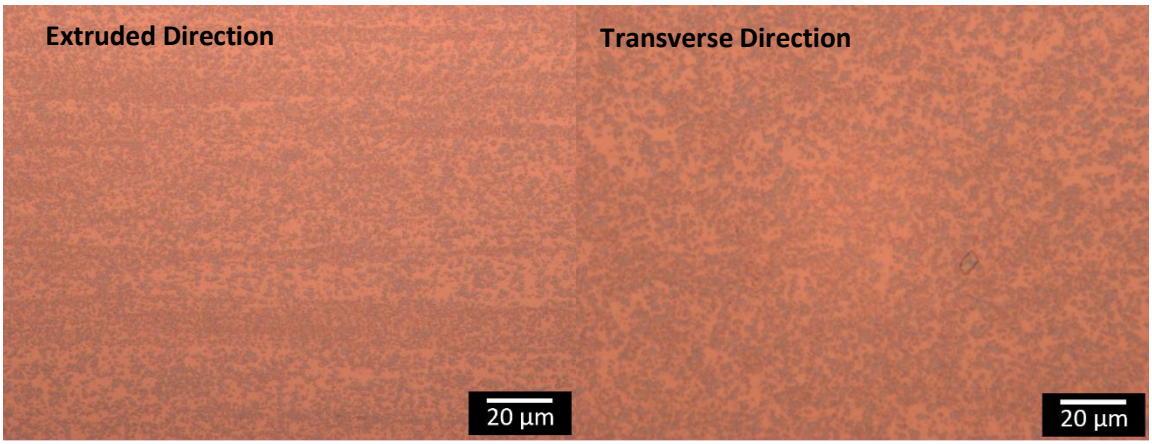

Figure 4.3: Representative Images for Directly Extruded GRCop-42.

Etched sample images obtained from optical microscopy were used to characterize and measure the grain size. Representative images in the etched state in both the XY and Z planes for each of the vendors are shown below in Figure 4.4 and Figure 4.5, respectively. The microstructure revealed during etching appears to be remnants of the melt pools generated during printing and not a refined grain structure. Due to this, the grain size of the specimens cannot be determined from the optical images. The volumetric defects indicated by circles provides evidence for lack of fusion defects in both the XY and Z planes for specimen A-2.

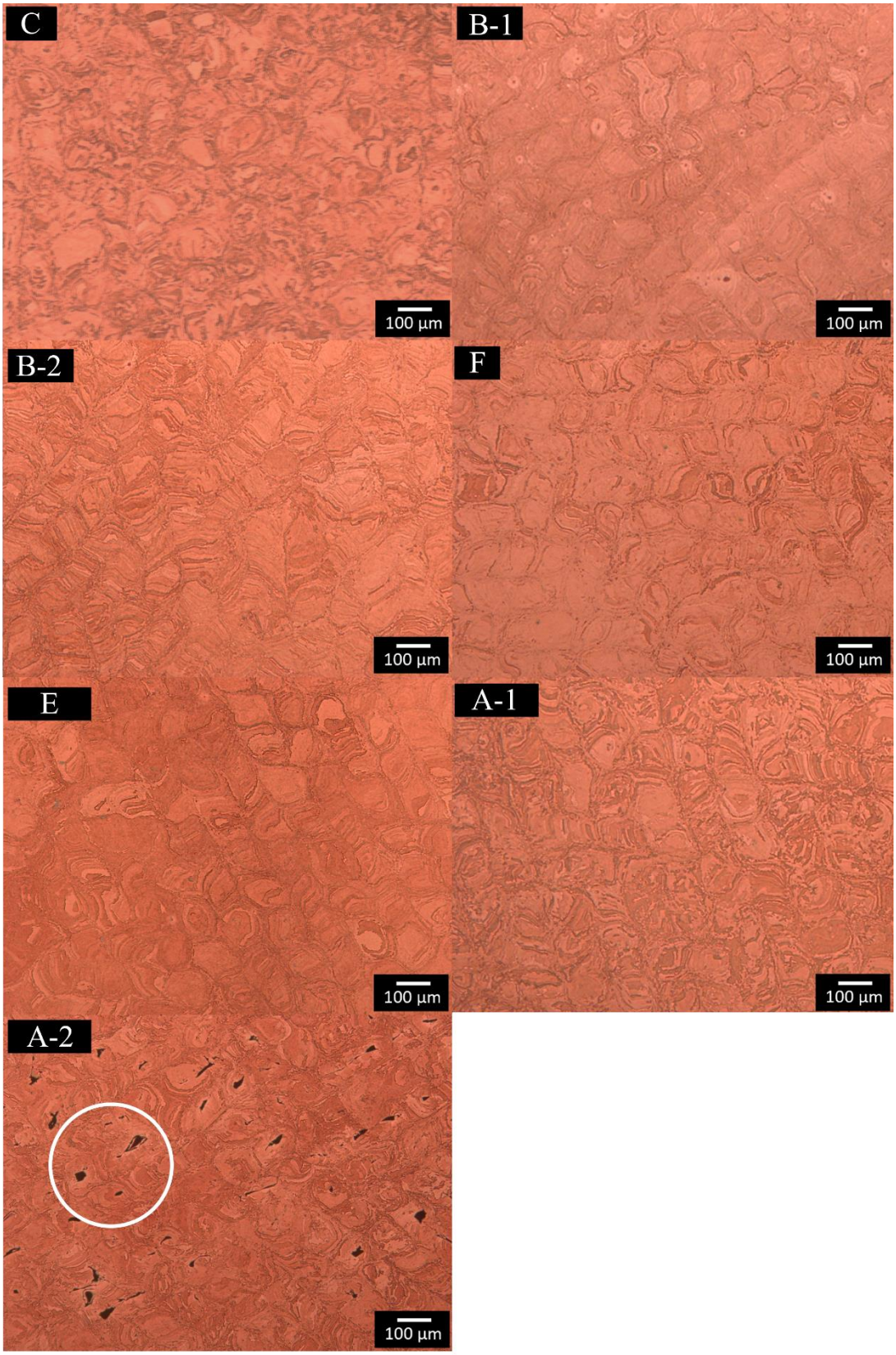

Figure 4.4: Etched Representative Images for Each Vendor in the XY Plane. Circles showing voids. Specimen ID in upper corner of each image.

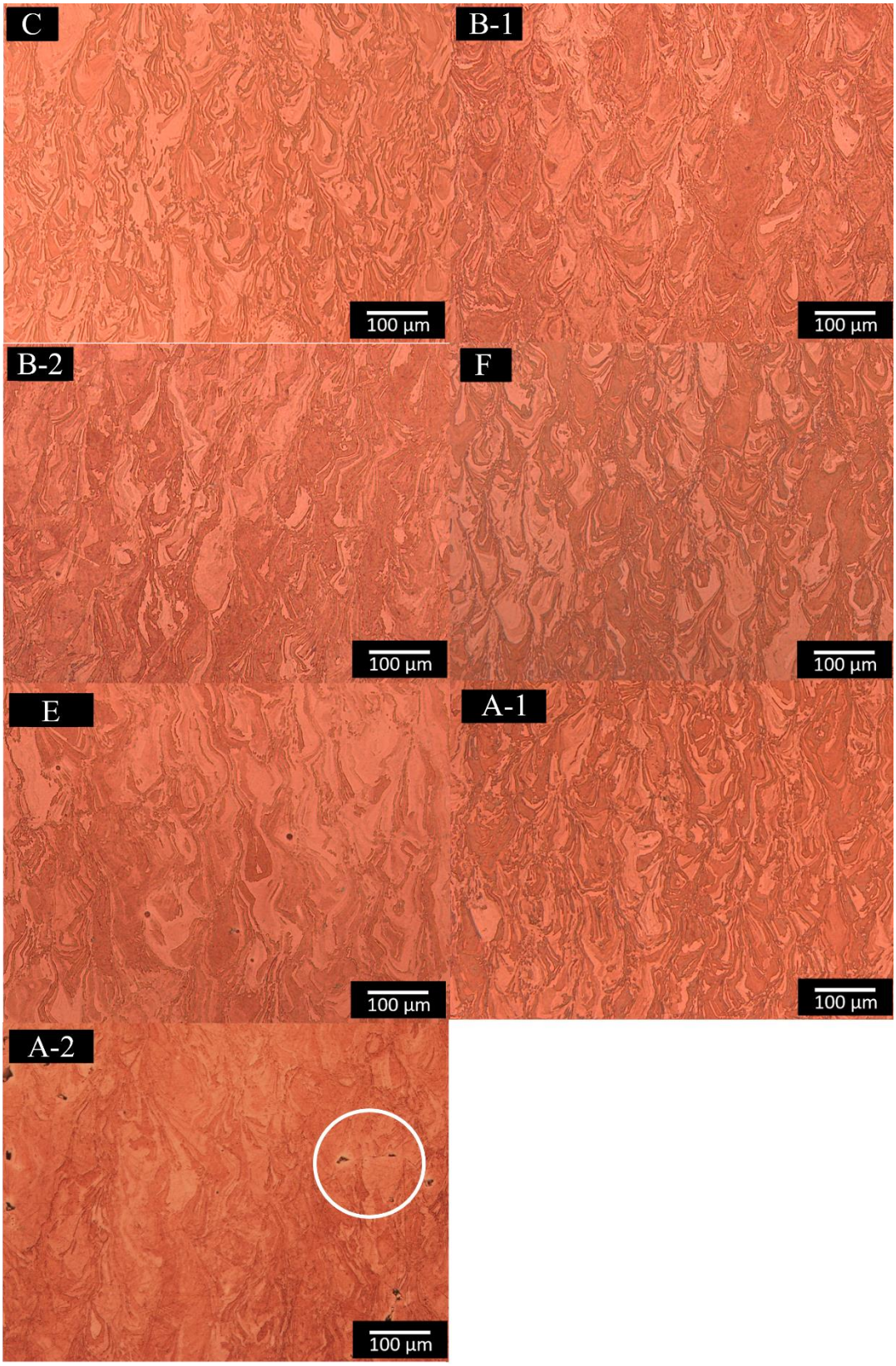

Figure 4.5: Representative Images for Each Vendor in the Z Plane. Circle showing voids. Specimen ID in upper corner of each image.

4.2 Dispersion Analysis

The images obtained from SEM taken in SEI imaging mode were used to conduct a dispersion analysis which measured the area fraction, feret diameter, and nearest neighbor distance (NND) of the dispersoids. The measured values are displayed in Table 4.1. Figure 4.6 depicts representative SEM images for both the (a) L-PBF and (b) DE samples. The DE samples dispersoids are made up of nanoscale Cr_2Nb particles that are agglomerated together as indicated by the white circle. These agglomerates are approximately the same size and distance apart from one another as the L-PBF dispersoids. The particles indicated by white arrows are polishing artifacts that were excluded from the dispersion analysis.

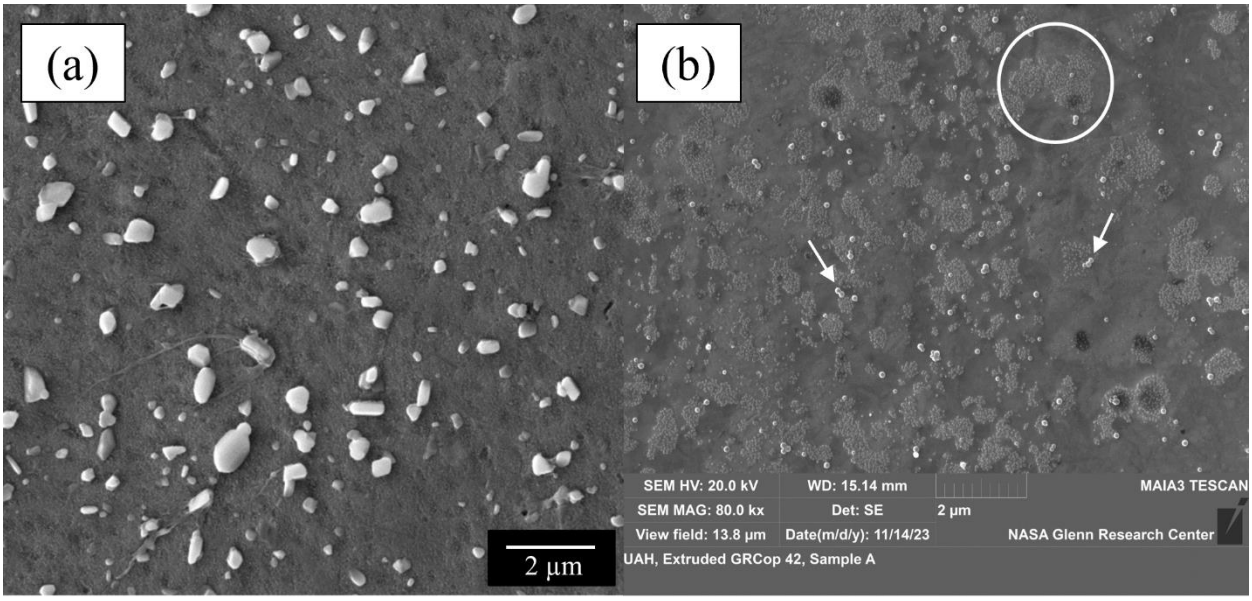

Figure 4.6: Representative SEM Images in SEI imaging mode for (a) L-PBF and (b) DE Samples. Circle indicates regions of clumped Cr2Nb particles that are equivalent in size to dispersoids in L-PBF. The arrows indicate particles related to polishing artifacts.

Table 4.1: Dispersion Size Analysis Results.

Identifier	Area Fraction (%)	Feret Diameter (μm)	NND (μm)
A-1	6.7	0.23 ± 0.22	0.37 ± 0.19
A-2	7.5	0.25 ± 0.25	0.38 ± 0.20
B-1	7.4	0.18 ± 0.16	0.27 ± 0.19
B-2	6.7	0.22 ± 0.21	0.36 ± 0.19
C	6.7	0.21 ± 0.22	0.35 ± 0.18
E	6.9	0.23 ± 0.18	0.29 ± 0.16
F	7.0	0.24 ± 0.22	0.38 ± 0.20
DE	5.6	0.25 ± 0.39	0.22 ± 0.26

There is minimal variation in dispersion size and distribution between each vendor. The measured area fraction for the dispersoids is close to the nominal 7%. Specimens A-2 and B-1 report slightly higher area fractions; however, this is to be expected as there was some preferential removal of Cu during the specimen preparation process. Even though each vendor used different machines and best practices the spread of the feret diameters and the NND is minimal which indicates adequate dispersoid distribution throughout the material for a wide variety of parameter sets. The measured area fraction for the DE sample is lower than the nominal expected value but this can be attributed to nano-sized precipitates that were unable to be resolved in SEM images.

4.3 Fractography

Initial fractography conducted in the Keyence VHX-7000 digital microscope revealed an unexpected feature, indicated by a blue circle, in vendor A's print as shown in Figure 4.7b. A representative sample is provided for comparison in Figure 4.7a.

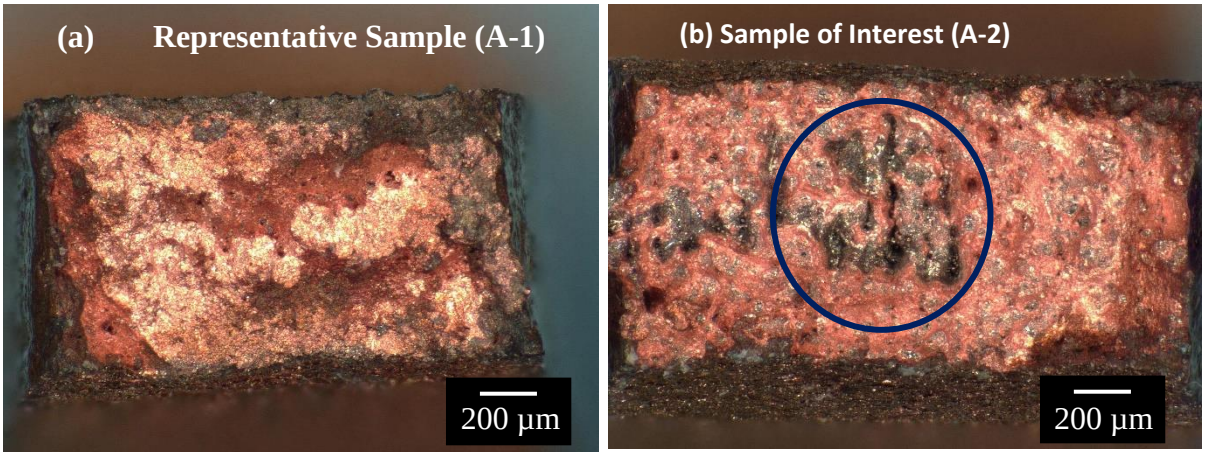

Figure 4.7: Keyence Fractography Representative Images for sample A-1 (a) and A-2 (b). Circle Indicates Feature of Interest.

On first inspection it appeared that there were large voids in the center of this tensile specimen which were not present in the other vendors' specimens. To determine if this feature was indeed voids, a profile measurement was taken as shown in Figure 4.8. The profile measurement revealed that there was some texturing to the fracture surface and possible voids, but further investigation was necessary.

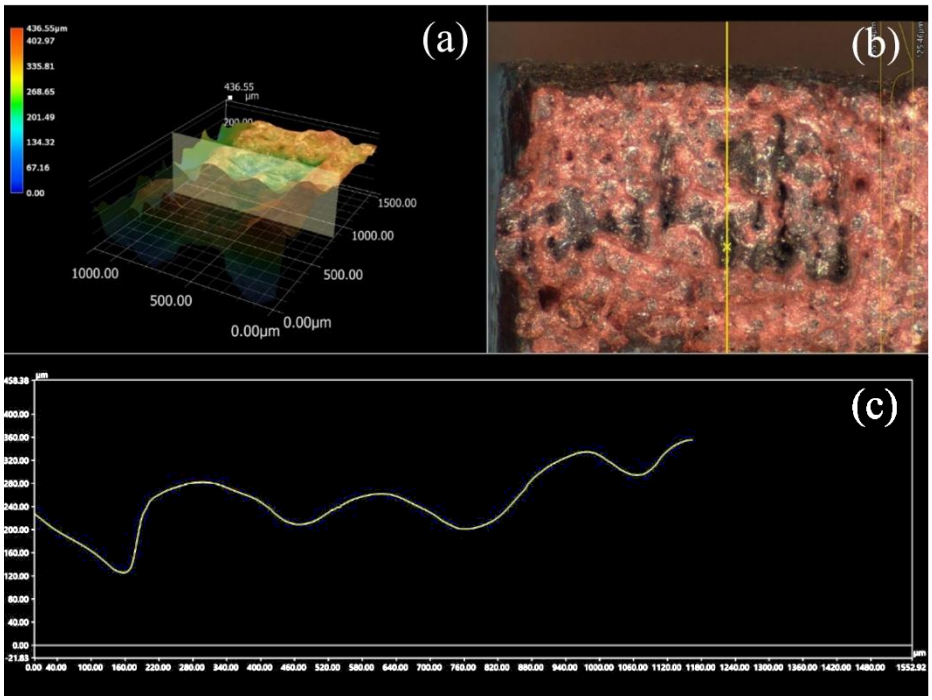

Figure 4.8: Profile Measurement across Specimen of Interest with (a) showing a 3D representation of the fracture specimen surface, (b) showing the location of the profile measurement and (c) showing the profile of the fracture surface.

To further identify the feature found in tensile specimen from vendor A-2, images of the entire fracture surface as well as higher magnification images of regions of interest were obtained and the location recorded for future reference. The same samples from Figure 4.7 are shown again in Figure 4.9.

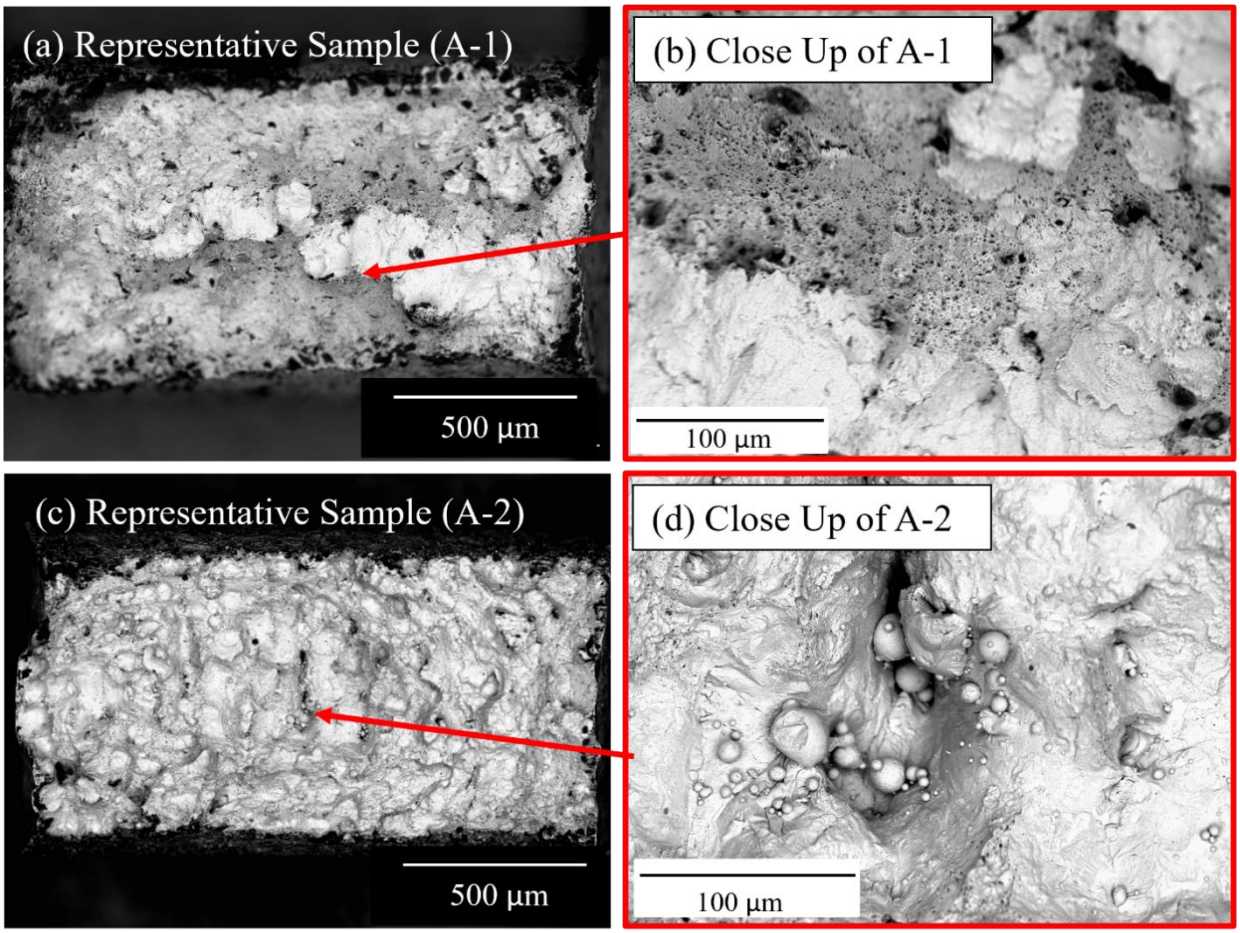

Figure 4.9: SEM Fracture Surface Images Taken in SEI Imaging Mode Showing Region of Interest for Specimen A-1 (a) with a close up in (b). Similar images are shown for specimen A-2 (c) with a close up in (d).

The "voids" that were present in the Keyence images for specimen A-2 appear to be regions of unmelted powder as the 30 µm round particles correspond to the initial size of the powder. The presence of unmelted powder corresponds to the lack of fusion throughout the specimens in vendor A-2.

4.4 Tension Testing

To summarize the tensile properties of each L-PBF build overhang, Figures 4.10, 4.11, and 4.12 display the ultimate tensile strength (UTS) as a grey bar, the yield strength (YS) as a red bar and the elongation as blue stars. To better compare across all build overhangs, Figure 4.13 presents the data as scatter plot.

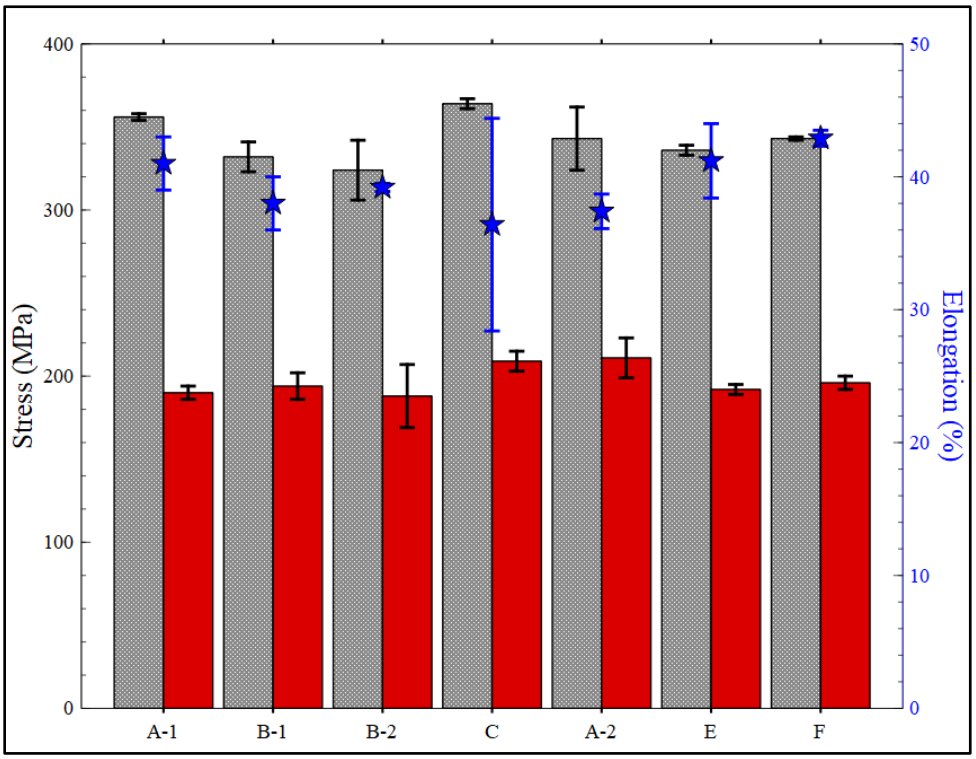

Figure 4.10: Mini-Tension Test Summary for 45° Overhang (UTS in Grey, YS in Red, Elongation in Blue).

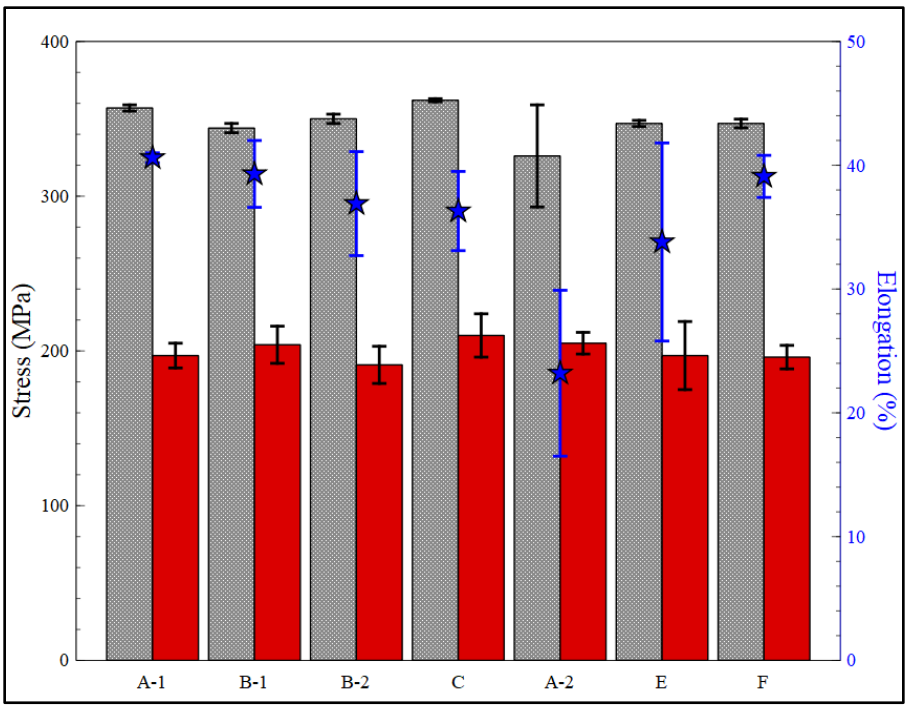

Figure 4.11: Mini-Tension Test Summary for 60° Overhang (UTS in Grey, YS in Red, Elongation in Blue).

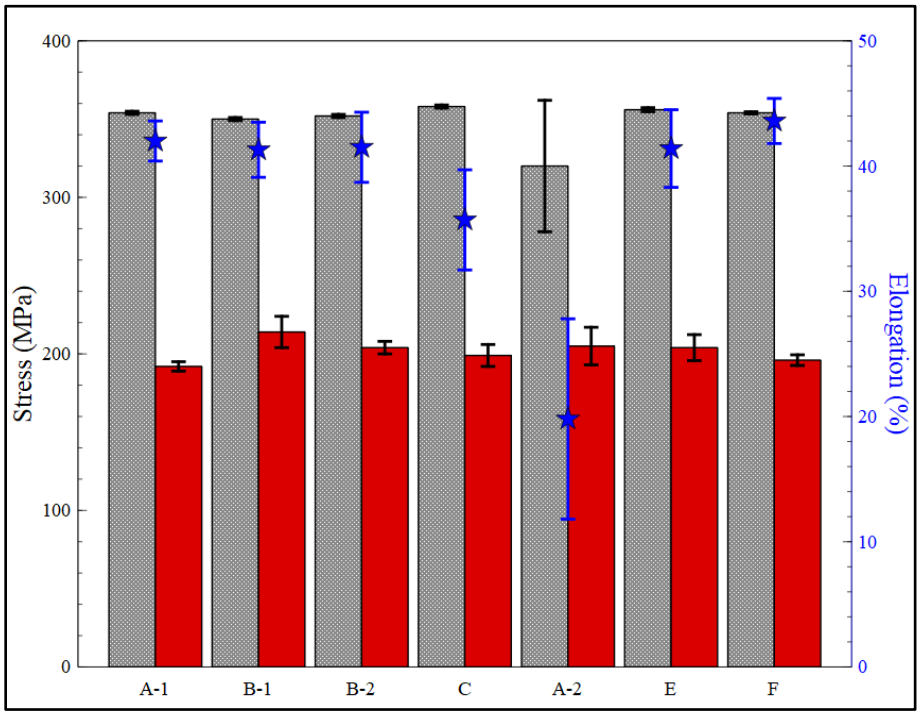

Figure 4.12: Mini-Tension Test Summary for 90° Overhang (UTS in Grey, YS in Red, Elongation in Blue).

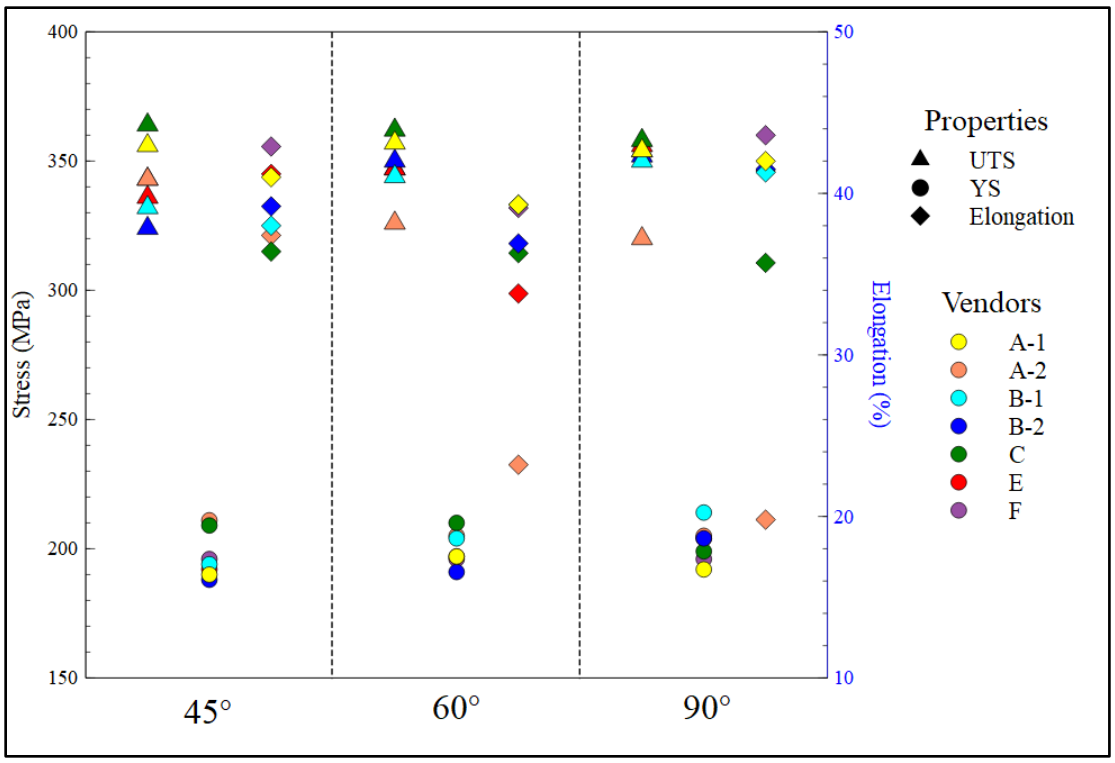

Figure 4.13: Summary of Tensile Data Across all Overhang Angles.

Looking individually at the various samples in the three overhang orientations highlights some differences. Figure 4.10 shows the most variability in the elongation for the C vendor in the 45° overhang samples. Whereas Figure 4.11 and 4.12 show more variability in the elongation for the A-2 vendor samples in the 60° and 90° overhang samples which is also reflected in Figure 4.13. Thus, these samples were investigated in greater detail.

Figure 4.14 compares the average across all the overhangs per vendor with properties from directly extruded GRCop-42. The grey bar is the UTS, the red bar is the YS, and the blue stars are the elongation. The L-PBF and directly extruded samples properties are equivalent. As noted in Figures 4.10 to 4.13, there is minimal variability except for specimens A-2 and C.

Average values of the mechanical properties of the L-PBF specimens are similar to that of the DE specimen.

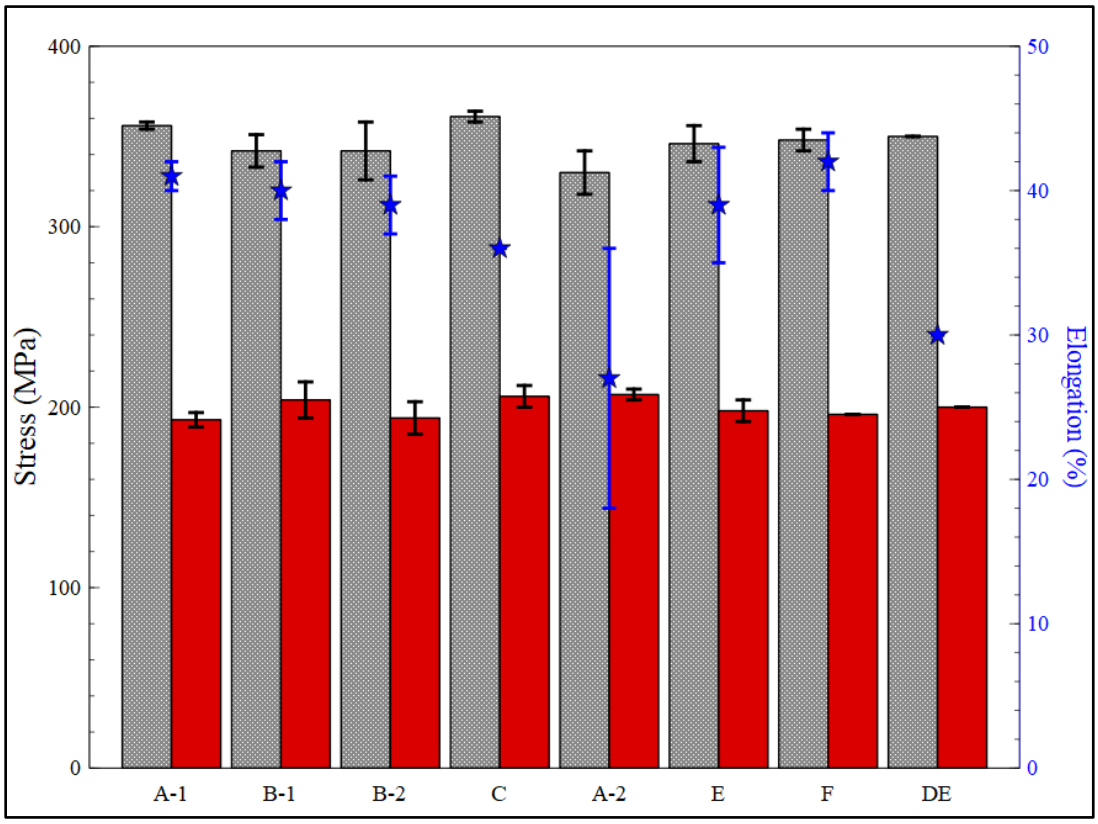

Figure 4.14: Average Properties for Each Vendor Compared to Directly Extruded Properties [11].

4.5 Electron Backscatter Diffraction (EBSD)

EBSD results for a representative L-PBF sample in the Z build direction are shown in Figure 4.15. Each color represents a different grain. Many pixels were not indexed, which may be due to either a fine grain size, grain boundaries or residual stress [32]. Using the grain boundary misorientation angle of 3°, Table 4.2 summarizes the average grain properties for the indexed samples of representative L-PBF GRCop-42 samples where ECD is the equivalent circle diameter.

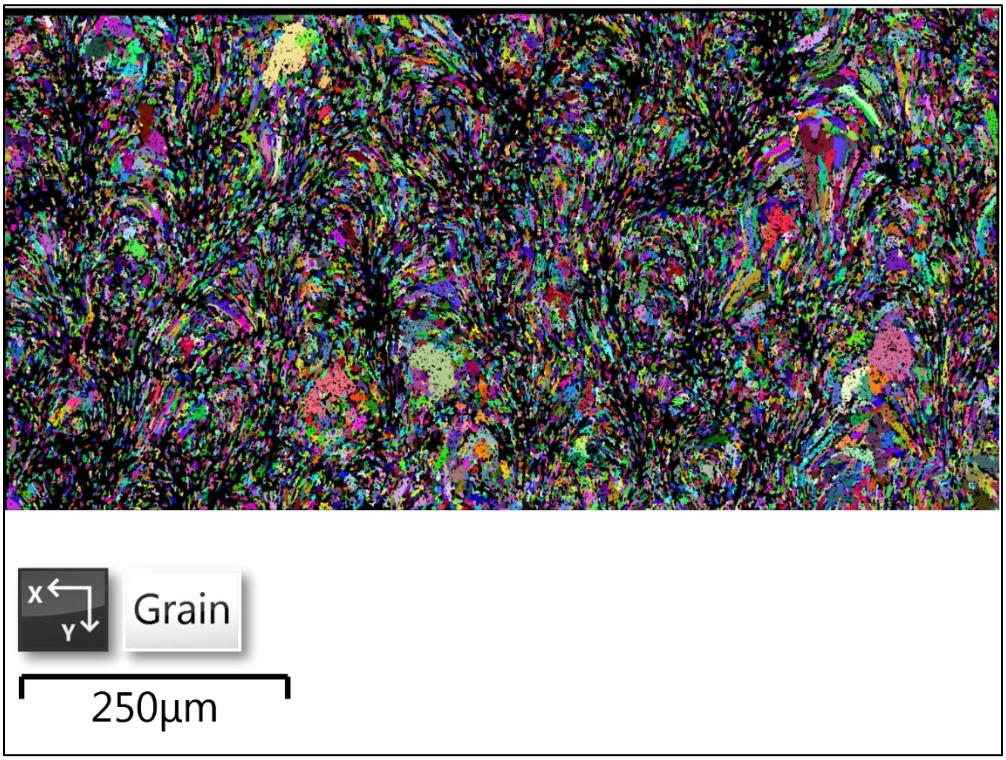

Figure 4.15: EBSD Random Color Grains for Representative L-PBF GRCop-42 [32].

Table 4.2: Grain Properties as Determined by Representative L-PBF EBSD [32].

Measurement	Minimum	Maximum	Mean
Area (µm^2)	6.4	1,392	15.93 ± 27.47
Aspect Ratio	1.04	11.32	2.2 ± 0.88
ECD (µm)	2.85	41.14	4.15 ± 1.76

4.6 X-Ray Diffraction (XRD)

XRD results are shown in Figure 4.16 for the L-PBF and DE samples. Table 4.3 summarizes the ICDD PDF files used for indexing of the phases present in the GRCop samples. Peak splitting can be observed in the Cu peaks of the L-PBF sample due to the difference in the Co-Kα_1 and Co-Kα_2 wavelengths of 1.789 nm and 1.79 nm, respectively. Due to peak broadening in the DE sample, peak splitting is not observed.

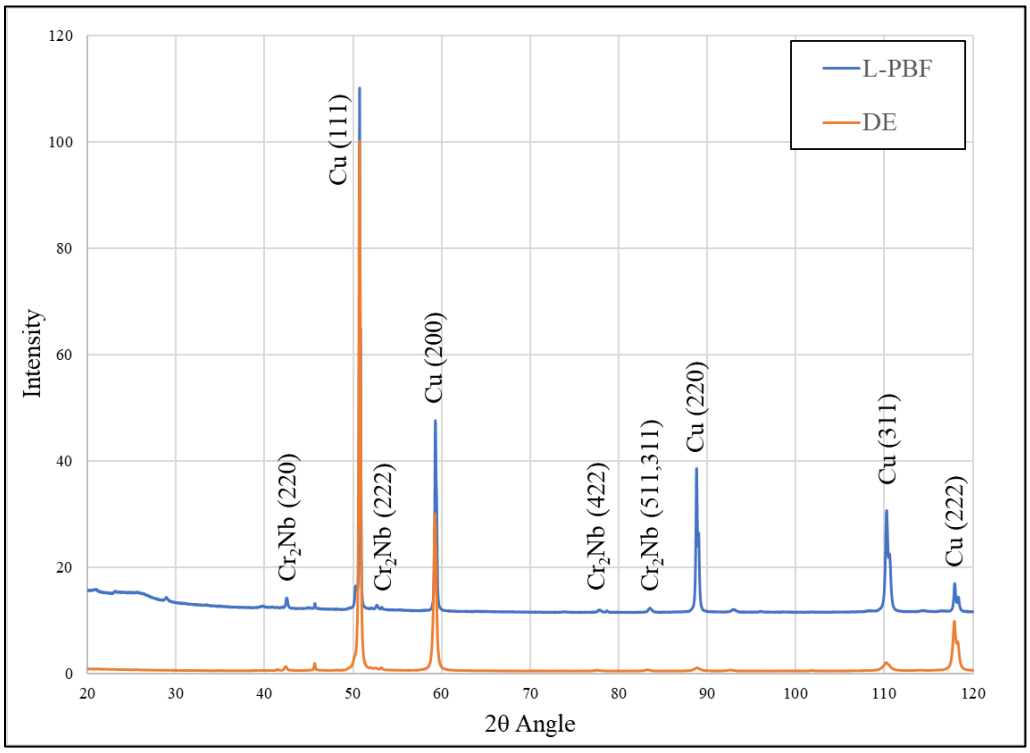

Figure 4.16: Comparison of XRD results over a 2θ range of 20°-120°.

Table 4.3: Summary of the ICDD PDF Files Used for Indexing the Phases Present in GRCop-42.

Element	Card ID
Cu	#006-4699
Cr2Nb	#01-071-7578
NbO	#00-043-1290

The intensity of the Cu peaks in the L-PBF sample aligns with the PDF file indicating a random texture. In contrast, the DE sample shows a slight preference for the (111) direction consistent with extrusion processing.

Figure 4.17 examines the first major Cu peak for both the L-PBF and DE samples and provides details about the both peaks' full width half max (FWHM) as well as highlights the presence of an NbO phase in the L-PBF samples that is not present in the DE sample. Both peaks are slightly shifted from the expected Cu peak at 50.79° for pure Cu powder. This can be due to either solute atoms present or residual stress in the sample.

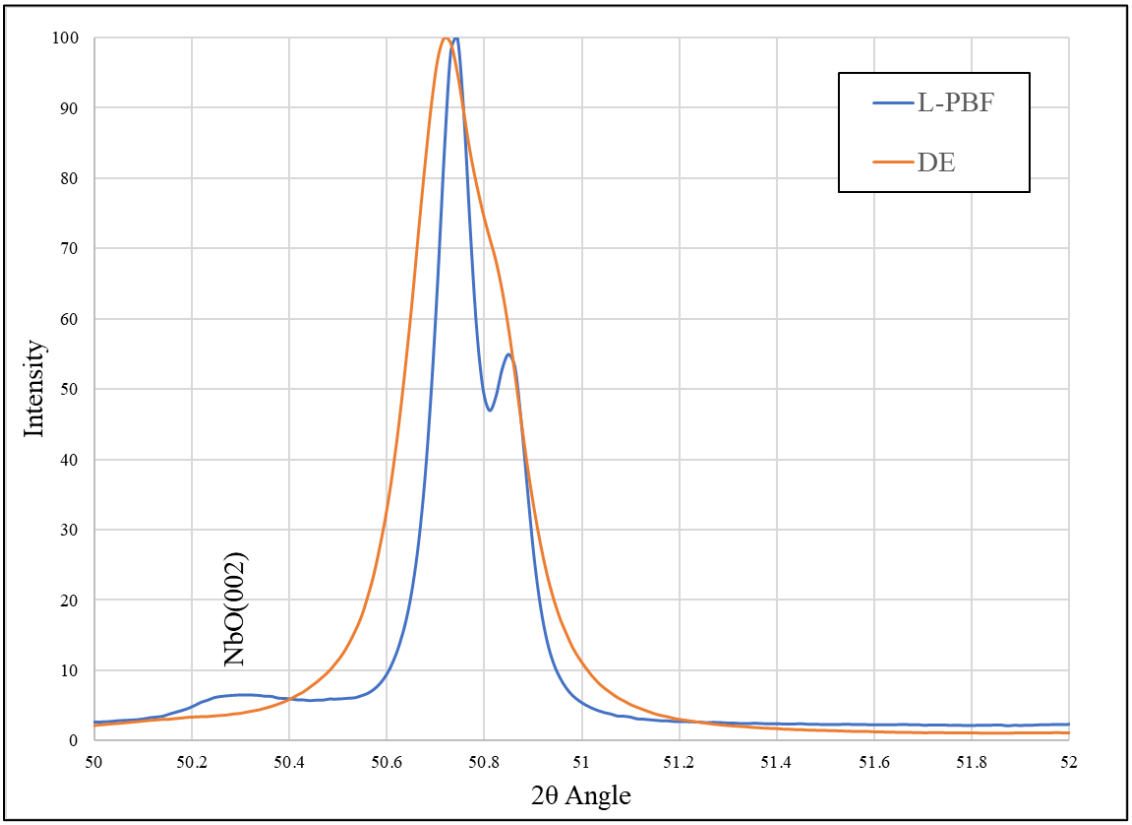

Figure 4.17: Close Up of Cu (111) Peak. Niobium Oxide (NbO) Phase Present in L-PBF sample but not DE Sample.

The FWHM peak width for the first Cu peak was measured for both specimens and their crystallite sizes calculated using the Scherrer equation as described in Equation 4 where β is the FWHM peak width, L is the crystallite size, θ is the Bragg angle, λ is the wavelength, and K is a

dimensionless shape factor considered to be 0.9 [33]. The calculated values are summarized in Table 4.4. The peak broadening indicates a smaller grain size for the direct extrusion sample. As each grain is made up of a mosaic of crystallites, the crystallite will be smaller than the grain size obtained by other methods. Typically, the boundaries of crystallites can be considered sub-boundaries and are usually separated by less than a 5° misorientation:

$$L = \frac{K\lambda}{\beta cos\theta}. \quad (4)$$

Table 4.4: Summary of Crystallite Size and FWHM Peak Width for L-PBF and DE Specimen.

Specimen	FWHM Peak Width (°)	Crystallite Size (nm)
L-PBF	0.183	558
DE	0.223	457

Chapter 5. Discussion

Based on this study, there appears to be a wide range of acceptable printing parameters that can be used to print GRCop-42 with sufficient tensile strength and ductility. The exception to this statement falls with vendors A-2 and C. Although the samples have sufficient strength as compared with the other L-PBF and DE samples, the reported ductility is 35% for specimen C and 20% for specimen A-2. This is much lower than the average of 40% elongation for the other samples in the study. To explain the reduced elongation values connections must be drawn between the analysis techniques presented in this study.

OM of each of the specimens revealed similar dispersoid size and NND across all vendors. Figure 5.1 compares the normalized powder, normalized scan speed, and energy density to the feret diameter and nearest neighbor distance of the various specimens in the study.

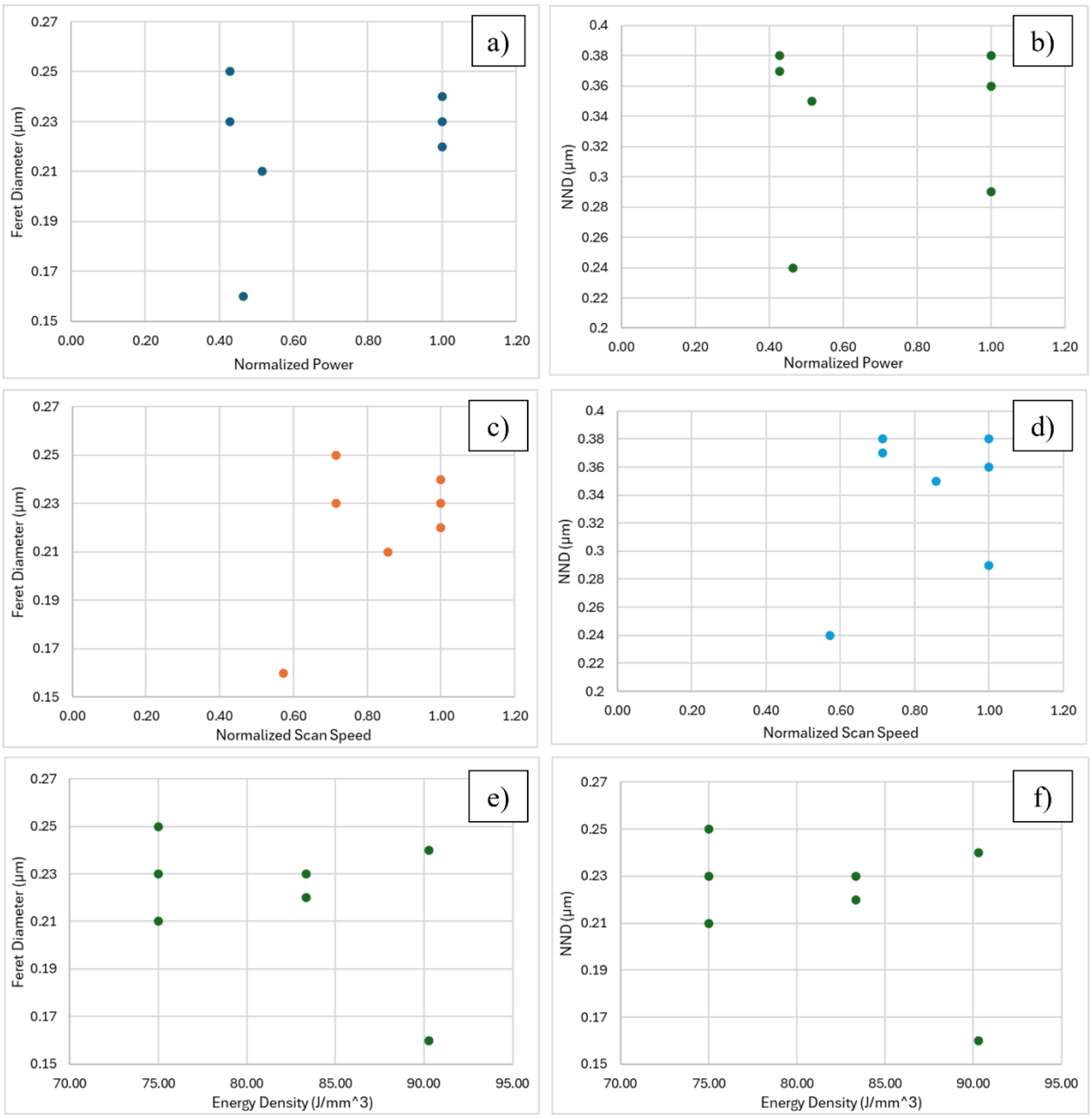

Figure 5.1: Comparison of a) power to feret diameter, b) power to NND, c) scan speed to feret diameter, d) scan speed to NND, e) energy density to feret diameter, and f) energy density to NND.

Although each vendor used parameters according to their best practice, this variety of parameters does not appear to influence the dispersoid size or NND in any predictable way. There are no visible trends between the power, scan speed and energy density and the

size/spacing of the dispersoids. This could be attributed to the small sample size of this study as there were only 7 sets of parameters that were used to generate feature build plate.

Although there is a homogeneous distribution of dispersoids throughout each specimen for most vendors, OM did reveal cracking and Cu rich regions in specimens A-2 and C. These Cu rich regions could possibly be regions of lack of fusion that were sealed up during the HIP process. Upon closer inspection, Tables 3.1 reveals that specimen A-2 and C used the lowest reported energy density of 75 J/mm^3. As this was the lowest reported energy density, and other vendors with higher energy densities did not show any volumetric defects, it can be inferred that 75 J/mm^3 is at the low end of an acceptable energy density parameter. By increasing the energy density, it is possible to mitigate any future lack of fusion[34].

Specimen A-1 also used the lowest reported energy density of 75 J/mm^3, however, no evidence of lack of fusion was present in the OM or fractography. The only remaining difference in the printing parameters between specimens A-1 and A-2 was the type of recoater blade used during printing. Specimen A-1 used a rubber recoater blade, and specimen A-2 used a steel recoater blade. As this was the only parameter changed between these two prints, a second explanation for specimen A-2's volumetric defects could lie in the interaction between the recoater blade and spatter generated during the print. Spatter occurs during most prints and can make the current build layer uneven. As the steel recoater blade moves across the build plate and encounter spatter, it cannot deform over it like a rubber recoater blade could. Powder then gets impacted into the leading side of the spatter which leaves less powder for the aft side therefore short dosing the print, Figure 5.2 depicts this phenomenon [34]. Once the laser begins to consolidate the layer, it cannot properly do so as the layer contains regions that are thicker and thinner than the nominal layer height. The laser is optimized for the nominal layer height

therefore this variability in layer height could impact the depth at which the laser penetrates resulting in volumetric defects such as lack of fusion [34,35].

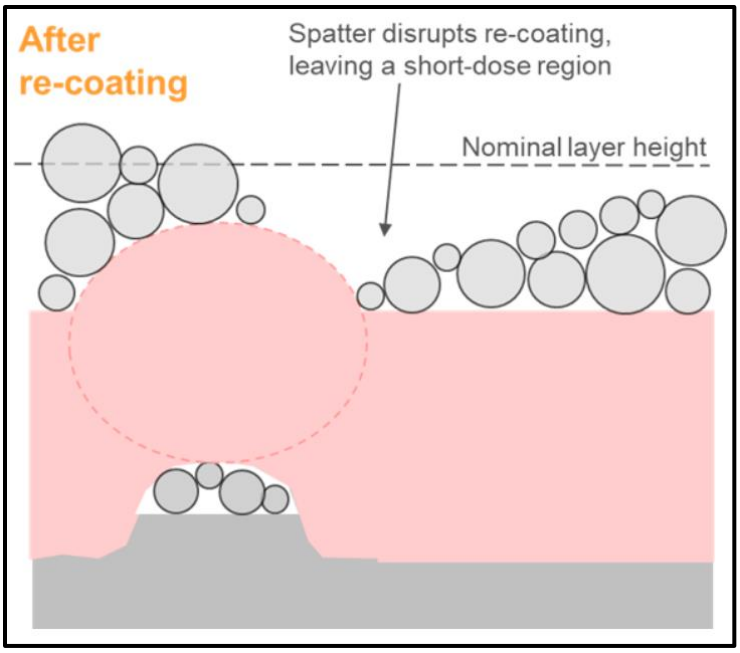

Figure 5.2: Example of Short Dosing During Wiper Blade Pass [36].

There are a variety of strengthening mechanisms that can be responsible for the observed strength in both the L-PBF and DE specimens. Equation 5 summarizes the various strengthening mechanisms that can be considered in this system which include the threshold stress, Hall-Petch strengthening, Orowan strengthening, precipitate strengthening, and solid solution strengthening respectively:

$$\sigma_y = \sigma_{th} + \Delta\sigma_{hp} + \Delta\sigma_{ow} + \Delta\sigma_{ppt} + \Delta\sigma_{ss}. \quad (5)$$

It has been reported, that for directly extruded GRCop-42, approximately 1/3rd of its strength comes from Orowan strengthening while the remaining 2/3rd comes from Hall-Petch strengthening [25]. Using this as a basis for comparison, the contribution from each of these strengthening mechanisms is estimated using the measured grain size of 4.15 µm from EBSD for the L-PBF specimen and the reported grain size of 1.53 µm for the DE GRCop-42 as well as the measured feret diameter for each specimen [37]. Using Equations 2 and 4, the contributions are

estimated, compared to the yield strength obtained from tension testing, and summarized in Table 5.1. Figure 5.3 compares the contributions from these two strengthening mechanisms to the reported ratio mentioned previously.

Table 5.1: Summary of Strengthening Mechanism Contribution in L-PBF and DE GRCop-42.

Specimen	Dispersion Strengthening (MPa)	Grain Size Strengthening (MPa)	Total Strengthening (MPa)	Measured Yield Strength (MPa)
L-PBF	48.3	85.1	133.4	200 ± 3
DE	47.0	123	170	200 [11]

Figure 5.3: Calculated Contributions from Strengthening Mechanisms Compared to Reported Ratio.

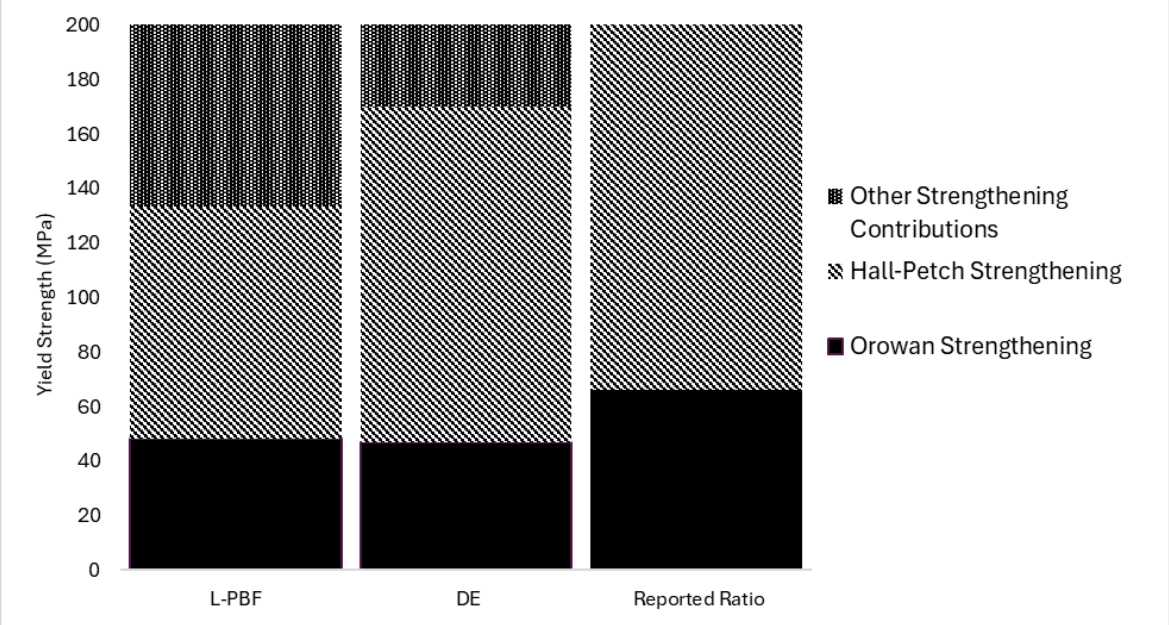

Since the dispersoids are similar in size between both processes, the contributions from Orowan strengthening are similar. The grain size of the L-PBF sample is approximately 4 times larger than the DE specimen therefore Hall-Petch strengthening contributes less to the L-PBF sample when compared to the DE sample. Both the L-PBF and DE process do not fit the reported ration exactly, as contributions from both strengthening mechanisms are less than the reported ratio.

When contributions from Orowan and Hall-Petch strengthening are summed together, it is apparent that there is more strengthening that's needs to be accounted for in both specimens but more extensively in the L-PBF sample. It has been reported that in other alloy systems, a fast cooling rate can increase the solubility of the alloying elements in the matrix [38]. Since L-PBF is a rapid solidification process, assuming this trend is also applicable to this alloy system, it would be expected that more precipitates could form a result of this increased solubility [39]. Due to the increase in precipitates, it would be within reason to expect more contributions from coherent precipitate strengthening in the L-PBF sample than in the DE sample as direct extrusion has a slower cooling rate when compared to L-PBF.

XRD of the L-PBF and DE samples revealed the presence of NbO in the L-PBF sample but not the DE sample. There are two possible sources for the oxide, either in preparation of the powder or from oxidation during the L-PBF process. It has been reported that when GRCop-42 is melted down in a ceramic crucible and at the high temperatures required for a uniform molten melt, the alumina refractories react with the Nb. This reaction promotes the generation of NbO which surrounds the sharp alumina particles. These particles can create stress concentration that could become crack nucleation sites [40]. During the L-PBF process, an inert gas is used to flow over the build plane to prevent oxidation. It is unknown how effective this is, although most vendors have an oxygen sensor to monitor for excess levels. This information was not reported in the various vendor reports who provided samples for this study. The NbO phase is not present in the DE material even though the material underwent a similar gas atomization process. The exact processing parameters for the powder used in the DE sample is unknown; therefore, it could have been melted in a nonceramic crucible therefore no alumina was introduced to the

alloy decreasing the chance of NbO formation. Additionally, the extrusion processing may have broken up any oxides to a level indistinguishable in XRD analysis.

Chapter 6. Summary

GRCop-42 is a robust material that can be manufactured in a variety of ways while still meeting tensile strength and ductility requirements. The following highlights the findings of this study:

- There is a wide range of acceptable L-PBF printing parameters that will generate GRCop-42 with properties equivalent to that of its heritage processing method of direct extrusion.
- The effect of printing parameters on the resulting melt pool had a minimal but not predictable effect of the size and NND of the dispersoids.
- A lower limit for the energy density of 75 J/mm^3 could be implemented to mitigate volumetric defects such as lack of fusion.
- Interactions between the steel recoater blade and spatter results in short dosing which leads to decreased elongation in specimens.
- The L-PBF process does not fit the expected ratio of strengthening mechanisms in the heritage DE process as the estimated contributions from both Orowan and Hall-Petch strengthening are less than what has been reported.
- Evidence suggests that there could be more contribution from coherent precipitate strengthening in the L-PBF sample as a faster cooling rate can increase the solubility of the alloying elements in the matrix.

Chapter 7. Future Work

Future studies exploring the interaction between the recoater blade and spatter could be conducted to further understand the impact of the L-PBF processing parameters on consolidated GRCop-42. By obtaining material from a variety of vendors while limiting the recoater blade type to a steel recoater blade, and controlling all other parameters, the interaction between the recoater blade and the spatter can be isolated. In addition, in-situ monitoring of spatter generation and location of spatter can be used to pinpoint regions of interest that could possibly contain volumetric defects because of recoater blade/spatter interactions. By isolating these parameters, influence from other parameters is minimized. These specimens can also be examined in the as-built condition to determine the depth at which the laser is penetrating the sample in regions where the layer height changes due to short dosing.

The effects of different additive processes on the resulting microstructure and mechanical properties of consolidated GRCop-42 must also be considered. Methods such as laser powder directed energy deposition (LP-DED) must be analyzed by obtaining builds similar to the L-PBF study printed using vendor best practices. By analyzing the feature builds, a set of acceptable parameters that generate GRCop-42 with sufficient tensile strength and ductility can be generated. Comparisons can also be drawn between the two different additive processes to showcase each method's effect on the resulting specimen's microstructure and mechanical properties.

It is recommended in further studies to preserve specimens with the final deposited layer. This will provide further information regarding the laser penetration depth, which will be helpful

in understanding the laser interaction between vendors. Additional details regarding the type of laser used and its wavelength is also recommended for future documentation.

Since there appears to be another strengthening mechanism present in the L-PBF samples, higher resolution imaging using transmission electron microscopy (TEM) is recommended. As solubility of alloying elements is increased as cooling rate increases [38], this has been reported to influence the formation of coherent strengthening precipitates, which could influence long term operation at elevated temperatures.

References

[1] German, R., “Powder Metallurgy and Particulate Materials Processing: The Processes, Materials, Products, Properties, and Applications,” Metal Powder Industries Federation, Princeton, New Jersey, 2005.

[2] Kelley F. C., “Powder Metallurgy,” *American Institute of Electrical Engineers*, Vol. 61, No. 9, 1942.

[3] Black, J. T., and Kohser, R. A., “Materials and Processes in Manufacturing,” 2008.

[4] Oliveira, J. P., LaLonde, A. D., and Ma, J., “Processing Parameters in Laser Powder Bed Fusion Metal Additive Manufacturing,” *Materials and Design*, Vol. 193, 2020. https://doi.org/10.1016/j.matdes.2020.108762

[5] Meyers, M., and Krishan, C., “Mechanical Behavior of Materials,” Cambridge University Press, 2009.

[6] ASM Handbook Committee, “Volume 2 Properties and Selection: Nonferrous Alloys and Special-Purpose Materials.”

[7] “MatWeb,” *https://matweb.com/, Access Date 1-30-2024*.

[8] Minneci, R. P., Lass, E. A., Bunn, J. R., Choo, H., and Rawn, C. J., “Copper-Based Alloys for Structural High-Heat-Flux Applications: A Review of Development, Properties, and Performance of Cu-Rich Cu–Cr–Nb Alloys,” *International Materials Reviews*, Vol. 66, No. 6, 2021, pp. 394–425. https://doi.org/10.1080/09506608.2020.1821485

[9] Ellis, D. L., “GRCop-84: A High-Temperature Copper Alloy for High-Heat-Flux Applications,” *NASA/TM-2005-213566*, 2005. http://www.sti.nasa.gov

[10] Ellis, D., “Conductivity of GRCop-42 Alloy Enhanced,” *NTRS, Research and Technology*, 2004.

[11] Gradl, P., Protz, C., Cooper, K., Garcia, C., Ellis, D., and Evans, L., “GRCop-42 Development and Hot-Fire Testing Using Additive Manufacturing Powder Bed Fusion for Channel-Cooled Combustion Chambers,” *AIAA/SAE/ASEE Joint Propulsion Conference*, 2019. https://doi.org/https://doi.org/10.2514/6.2019-4228

[12] Walker, E. D., “The Stability of the Dispersion Stregthening Mechanism in Additively Manufactured GRCop-42,” Honors Capstone. University of Alabama in Huntsville, Huntsville, 2022.

[13] Dieter, G. Ellwood., and Bacon, D. J., “Mechanical Metallurgy,” McGraw-Hill, New York, 1988.

[14] Chua, A., “Development of Aluminum Powder Metallurgy Alloys for Aerospace Applications,” Dalhousie University, 2014.

[15] Abu-Lebdeh, T., Leon, G. P., Hamoush, S. A., Seals, R. D., and Lamberti, V. E., “Gas Atomization of Molten Metal: Part II. Applications,” *American Journal of Engineering and Applied Sciences*, Vol. 9, No. 2, 2016, pp. 334–349. https://doi.org/https://doi.org/10.3844/AJEASSP.2016.334.349

[16] Callister, W., and Rethwisch, D., “Fundamentals of Materials Science and Engineering,” Vol. Fifth Edition, 2018.

[17] Dieter, G. E. J., “Mechanical Metallurgy and Metallurgical Engineering Series,” McGraw-Hill Book Company, 1961. https://doi.org/07-016890-3

[18] Porter, D. A., “Phase Transformations in Metals and Alloys,” CRC Press, 2022.

[19] Baker, H., and Okamoto, H., Eds., “ASM Handbook,” 1992.

[20] Henry C de Groh III, David L. Ellis, and William S. Lowenthal, “Comparison of GRCop-42 to Other High Thermal Conductive Cu Alloys,” *NASA/TM 2007-214663*, 2007.

[21] Lee, Y. [, and Vafai, K. [, “Comparative Analysis of Jet Impingement and Microchannel Cooling for High Heat Flux Applications,” *International Journal of Heat and Mass Transfer*, Vol. 42, 1999, pp. 1555–1568.

[22] Rezayat, M., Karamimoghadam, M., Ashkani, O., and Bodaghi, M., “Characterization and Optimization of Cu-Al2O3 Nanocomposites Synthesized via High Energy Planetary Milling: A Morphological and Structural Study,” *Journal of Composites Science*, Vol. 7, No. 7, 2023. https://doi.org/10.3390/jcs7070300

[23] Shukla, A. K., Narayana Murty, S. V. S., Sharma, S. C., and Mondal, K., “Aging Behavior and Microstructural Stability of a Cu-8Cr-4Nb Alloy,” *Journal of Alloys and Compounds*, Vol. 590, 2014, pp. 514–525. https://doi.org/10.1016/j.jallcom.2013.12.057

[24] Ellis, D. L., Michal, G. M., and Dreshfield, R. L., “A New Cu-8 Cr-4 Nb Alloy for High Temperature Applications,” *NASA/TM-1995-106910*, 1995.

[25] Anderson, K. R., “High Temperature Coarsening of Cr2Nb Precipitates in Cu-8 Cr-4 Nb Alloy,” University of California at Davis, Davis, 1996.

[26] Hansen, N., “Hall-Petch Relation and Boundary Strengthening,” *Scripta Materialia*, Vol. 51, No. 8 SPEC. ISS., 2004, pp. 801–806. https://doi.org/10.1016/j.scriptamat.2004.06.002

[27] Hull, D., and bacon, D. J., “Introduction to Dislocations,” Elsevier Butterworth-Heinemann, Burlington, 2001.

[28] Gladman, T., “Precipitation Hardening in Metals,” *Materials Science and Technology*, Vol. 15, No. 1, 1999.

[29] Kumar, A., Bai, Y., Eklund, A., and Williams, C. B., “Effects of Hot Isostatic Pressing on Copper Parts Fabricated via Binder Jetting,” Vol. 10, 2017, pp. 935–944. https://doi.org/10.1016/j.promfg.2017.07.084

[30] “Touchstone Testing Labs,” https://www.touchstonetesting.com/, Access Date 1-30-2024.

[31] “ImageJ,” https://imagej.net/ij/, Access Date 1/30/2024, Version 2.15.1, 2022.

[32] Ellis, D., “EBSD Results with Representative Figures,” *Internal NASA-GRC Publication*, 2023.

[33] Langford, J. I., and Wilson, A. J. C., “Seherrer after Sixty Years: A Survey and Some New Results in the Determination of Crystallite Size,” 1978.

[34] Simpson, J., and Dehoff, R., “Review of Advanced Manufacturing Techniques and Qualification Processes for Light Water Reactors-Laser Powder Bed Fusion Additive Manufacturing,” *Task Order 1310018F0058 M0001*, 2020. www.osti.gov

[35] Reijonen, J., Revuelta, A., Metsä-Kortelainen, S., and Salminen, A., “Effect of Hard and Soft Re-Coater Blade on Porosity and Processability of Thin Walls and Overhangs in Laser Powder Bed Fusion Additive Manufacturing,” *International Journal of Advanced Manufacturing Technology*, Vol. 130, Nos. 5–6, 2024, pp. 2283–2296. https://doi.org/10.1007/s00170-023-12853-5

[36] Marc Saunders, “Spatter Matters,” *Linked in Article*, 2018.

[37] Anderson, K. R., “Effects of Thermal and Mechanical Processing on Microstructures and Desired Properties of Particle-Strengthened Cu-Cr-Nb Alloys,” 2000.

[38] Belov, N. A., Eskin, D. G., and Aksenov, A. A., “Multicomponent Phase Diagrams: Applications for Commercial Aluminum Alloys,” Elsevier, Boston, 2005.

[39] Lass, E. A., Stoudt, M. R., Williams, M. E., Katz, M. B., Levine, L. E., Phan, T. Q., Gnaeupel-Herold, T. H., and Ng, D. S., “Formation of the Ni3Nb δ-Phase in Stress-

Relieved Inconel 625 Produced via Laser Powder-Bed Fusion Additive Manufacturing," *Metallurgical and Materials Transactions A: Physical Metallurgy and Materials Science*, Vol. 48, No. 11, 2017, pp. 5547–5558. https://doi.org/10.1007/s11661-017-4304-6

[40] Jennings, W. D., and Ellis, D. L., "Characterization of Additively Manufactured GRCop-42 And GRCop-84," *Society of Applied Spectroscopy, 65th Annual May Meeting*, 2023.